Chapter

4 *Validation II: Results and Analysis*

"And so we see that the poetry fades out of the problem, and by the time the serious application of the exact science begins we are left with only pointer readings."

EDDINGTON

This chapter presents the results for the validation of the *Radiance* illuminance calculation. Predictions for external and internal illuminances are compared first with measurements. Next, the error characteristics of the internal illuminance predictions are analysed in detail, and the hypothesis concerning the source visibility related errors is tested. The preparatory work for the validation was described in the previous chapter.

4.1 External illuminance predictions

The first test of the validation exercise was a comparison of predictions for external illuminances with measurements. Global horizontal illuminance and the four vertical illuminances were measured independently of the sky luminance distribution. The comparison therefore served as a first stage 'quality assurance' test. Plainly, any major discrepancies here would

indicate that there were gross errors in either the validation data and/or the processing of the sky luminance measurements - the intrinsic accuracy of the *Radiance* illuminance calculation for this relatively trivial task is not an issue.[1] In the absence of input data errors, it was to be expected that the external illuminance could be predicted to a reasonably high degree of accuracy. The ambient parameter combination used to predict the external quantities is given in Table 4-1. The *Radiance* scene for these simulations contained only the sky description - the office model was not required and so it was excluded. Surfaces across which irradiance interpolation may occur were therefore not present in the scene, and so the simulation was insensitive to the value of the **ar** and **aa** ambient parameters. The ambient value (**av**) was of course set to zero. The *Radiance* simulations for this test were managed using the automation scheme outlined in Section 3.3.4.

Parameter	Value
ad	1024
as	256
ab	1

Table 4-1. Ambient parameters for external illuminance predictions

4.1.1 Results and discussion

The relative error in the illuminance predictions for the global horizontal and the four total vertical quantities are shown as frequency histograms in Figure 4-1. In each case, the bin size was 1% and the distribution was normalised to total = 1. As expected, the relative errors in the predictions for global horizontal illuminance were very low.[2] They were not however exact: the peak of the distribution was in the range -1.5% to -0.5% and the MBE was -0.7%. This slight negative bias was despite the fact that the (model) sky luminance distribution was normalised to the diffuse horizontal illuminance.[3] For the total vertical quantities the predictions were as

1. See example Section 2.3.3.

2. The relative error (RER), the mean bias error (MBE) and the root mean square error (RMSE) are defined Appendix A.

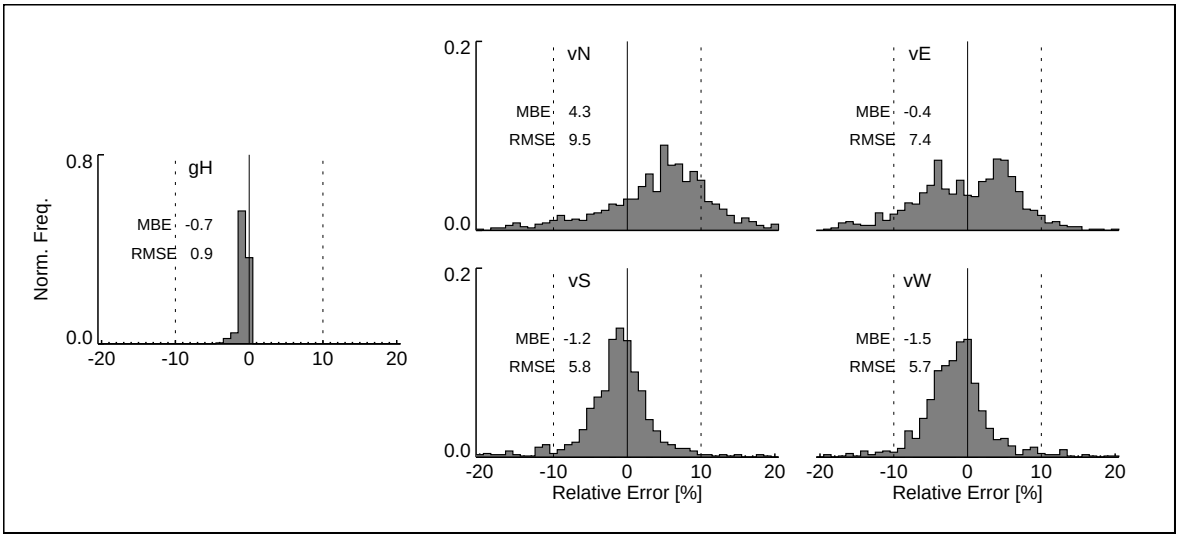

Figure 4-1. Predictions for total vertical illuminances

follows. Vertical north showed a positive bias (MBE = 4.3%) and moderate scatter (RMSE = 9.5%). The distributions in the RERs for vertical south and west were nearly identical - MBEs were 1.2% and 1.5% and RMSEs were 5.8% and 5.7% for south and west respectively. The distribution in RER for vertical east was bimodal with a negative and a positive peak at (approx.) -5% and 5%. The MBE for this orientation was very small (-0.4%), but the scatter (RMSE = 7.4%) was larger than that for vertical south and west.

Some of the features of these RER distributions can be attributed to underestimation of the circumsolar sky luminance. Recall that the circumsolar sky luminance was not measured by the scanner and so it had to be estimated using interpolation (Section 3.2.5). As described in that section, the interpolation could not reliably reproduce the high luminances of the sky about the circumsolar region (for non-overcast days). Furthermore, when this occurs, the normalisation will then reset the other sky luminances to a slightly higher value to offset the under-prediction in the circumsolar luminance (see Figure 3-23 on page 76). This effect may be manifest in the predictions for the vertical illuminances as follows. For those

3. This results from the finite-element approximation used for the normalisation.

instances when the sky was clear and the sun was in the south, under-prediction of the sky component (i.e. circumsolar sky luminance) of illuminance for vertical south will be associated with over-prediction of the sky component of illuminance for vertical north. When this situation occurs, it is likely to show up in the RERs as an over-prediction for vertical north, but not necessarily as an under-prediction for vertical south. This is because the (total) vertical south illuminance has, for the scenario described above, components of sky and (direct) sun illuminance. Whereas the (total) vertical north illuminance is that due to the sky only. The propensity for the under-prediction of the (total) vertical south illuminance was greatest for clear sky conditions. But for these instances, the direct sun component of the total vertical south illuminance was large - thereby minimising the effect of the (proposed) under-estimation of the circumsolar sky luminance. This effect is seen in some of the plots below where the RER in the predictions for the four total vertical illuminances is shown alongside a time-series of the measured four total vertical illuminances, with direct normal illuminance also, Figure 4-2 - Figure 4-5. The days when it was most apparent were 102_92, 125_92, 127_92 and 128_92 (all Figure 4-2). This effect may also be the reason for the small negative bias in the RER distribution for vS and the larger positive bias in the RER distribution for vN (Figure 4-1).

There were other patterns in the RER time-series plots for vertical illuminance that cannot be explained in terms of under-estimation of the circumsolar luminance. However, they clearly have some relation to the angle between the sun and the vertical plane surface normal. For example, there were distinct ‘blips’ in the RER time-series that were associated with sun azimuth angles of (approx.) 180˚ and 270˚. At these azimuths, the sun ‘switches’ from just illuminating one vertical plane, e.g. east, to just illuminating the ‘opposite’ plane, i.e. west. For example, the east-west switch is associated with noticeable ‘blips’ at times (approx.) 137_92_12h00 and 318_92_12h00. The ‘blips’ associated with the north-south switch

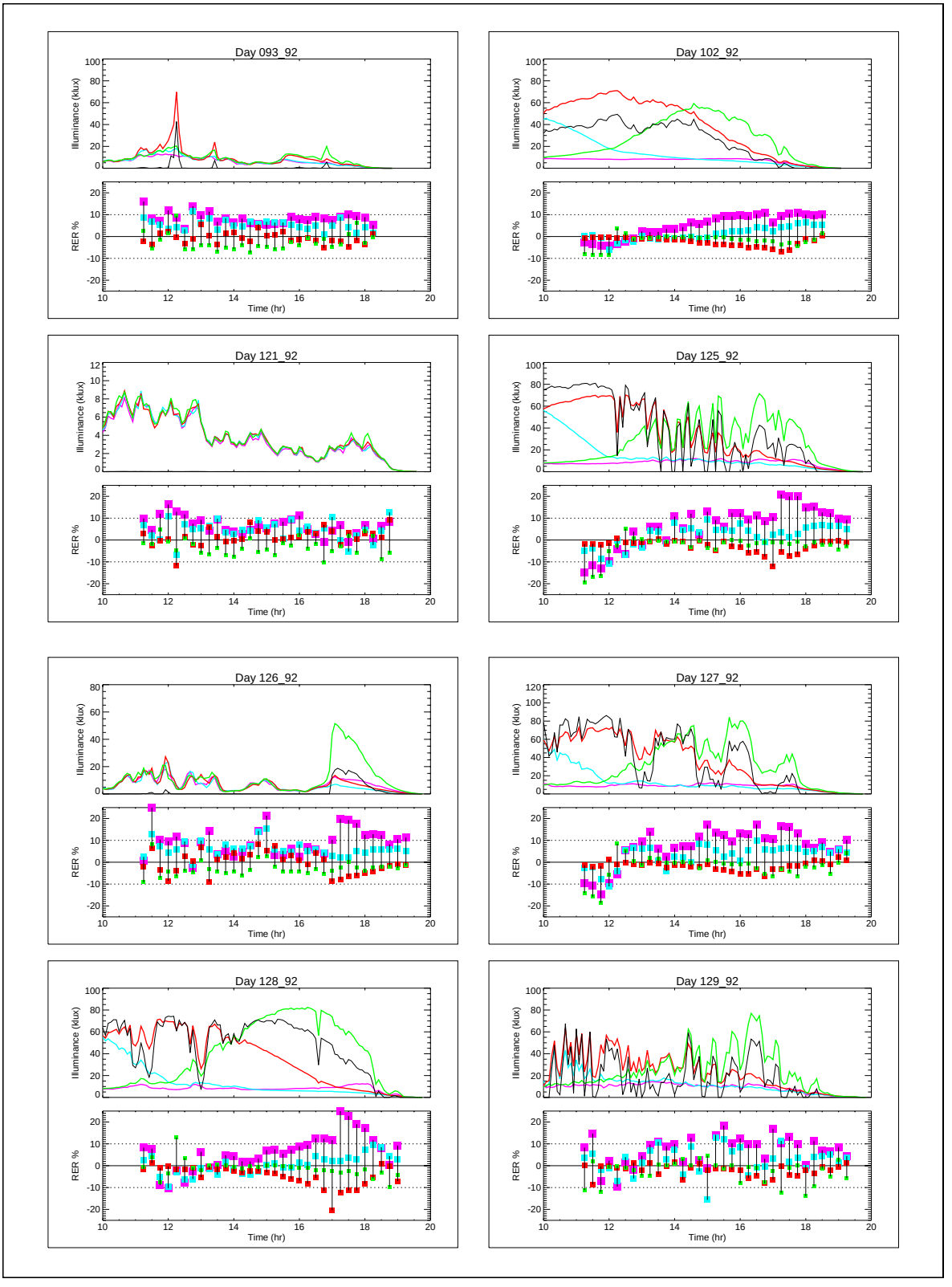

Figure 4-2. Vertical illuminance RER time-series

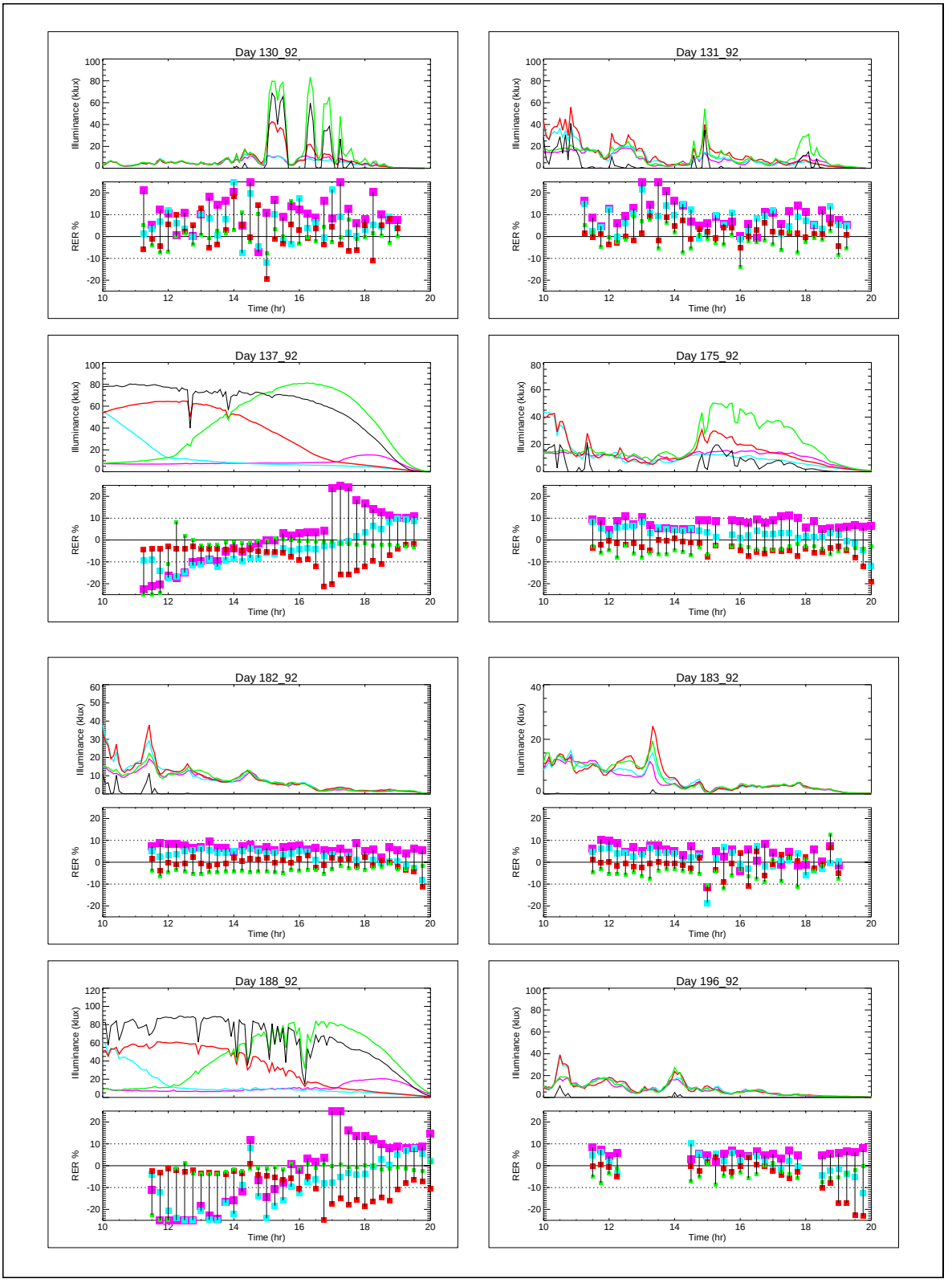

Figure 4-3. Vertical illuminance RER time-series

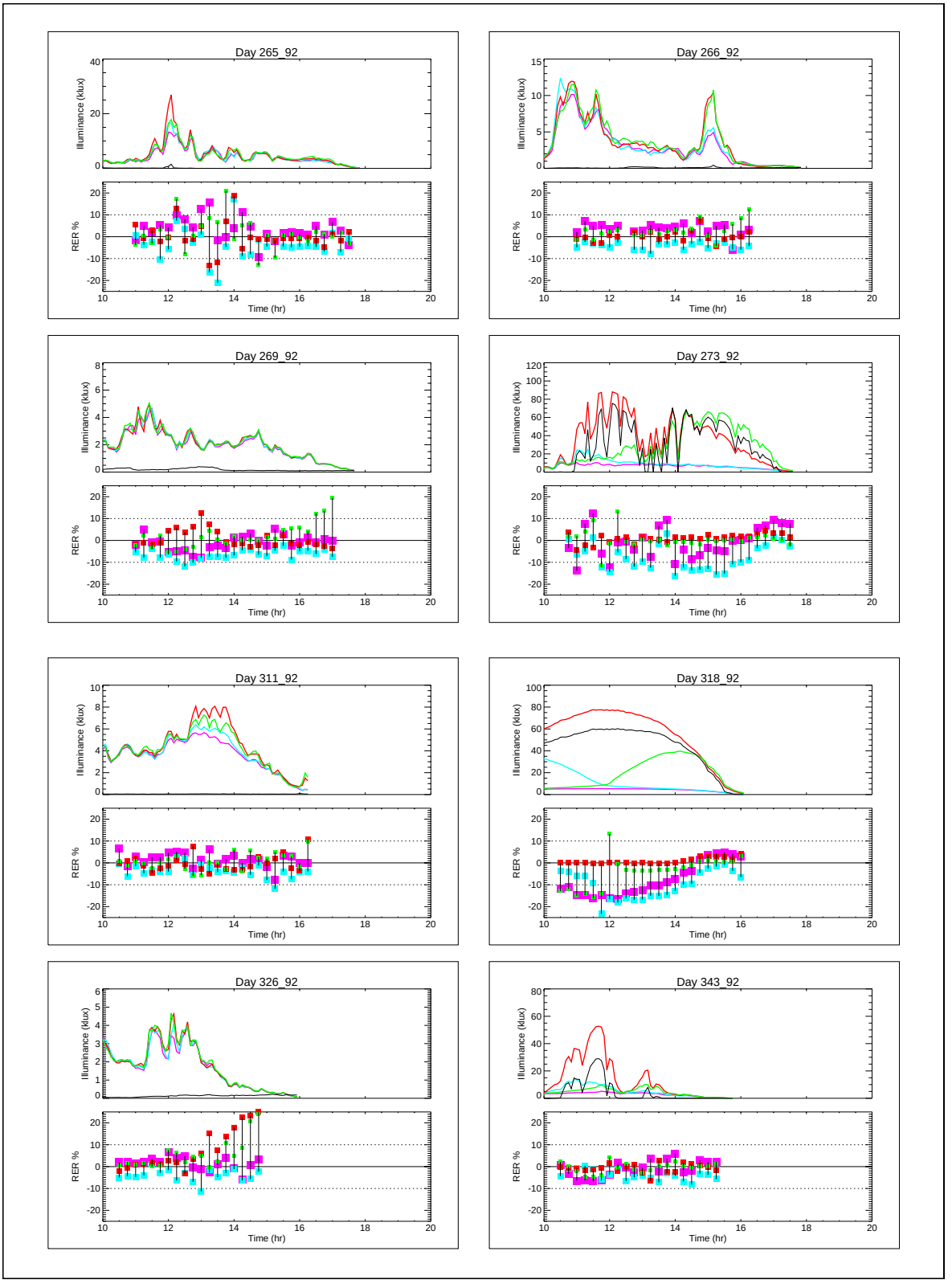

Figure 4-4. Vertical illuminance RER time-series

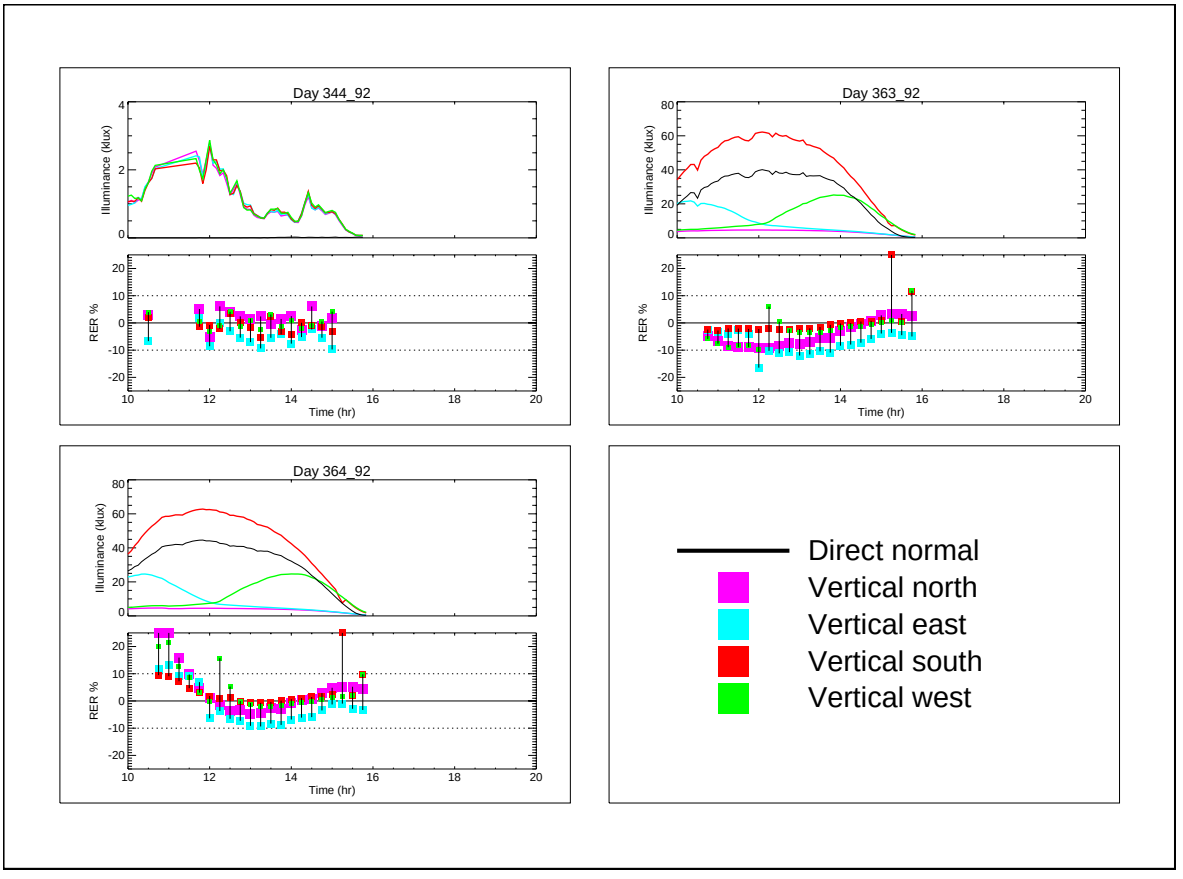

Figure 4-5. Vertical illuminance RER time-series

appear even more pronounced, e.g. 128_92_17h00, 137_92_17h00 and 188_92_17h00. Note also that for all the clear sky days, the pattern in the RER time-series exhibits sinusoidal-like features: 102_92 and 128_92 (Figure 4-2); 137_92 and 188_92 (Figure 4-3); 318_92 (Figure 4-4) and 363_92 and 364_92 (Figure 4-5). These patterns are very distinct, and because they only occur for clear skies it is highly likely that they are related in some way to the sun position.

4.2 Internal illuminance predictions

4.2.1 Individual cases

Internal illuminance predictions for a handful of skies were obtained prior to carrying out the simulations for all the 754 skies in the validation

dataset. This was to demonstrate that the modelling approach was sound and also to carry out a limited test for two of the innovative glazing types. Detailed comparisons between measurement and predictions are presented for four cases: two for ordinary glazing, one for the diffuse light shelf and one for the mirror light shelf. Table 4-2 gives a brief description of the measured skies and the glazing type modelled for the office.

Day-time-year	Solar altitude	Solar azimuth	Sky type	Innov. glazing fixture
102_92_13h00	45.5	201.4	Sunny - intermediate	-
121_92_14h15	44.3	230.1	Dull - overcast	-
137_92_12h00	57.7	181.8	Sunny - intermediate	Diffuse light shelf
318_92_12h00	19.8	184.0	Sunny - intermediate	Mirror light shelf

Table 4-2. Summary of sky conditions and glazing type

The results for the four cases are given in Figure 4-6 and Figure 4-7. Each of the figures shows the following:

- a plot of the measured and predicted illuminance at the six photocell locations (logarithmic scaling);
- a histogram of the relative error in the predictions; and,
- a wire-line surface plot of the (model) sky luminance distribution with a perspective-aligned contour plot of same.

The predictions for all the skies, glazing fixtures and photocell locations show good agreement with measurement. For all 24 (6 x 4) illuminance predictions, the mean error was 5.6% with a standard deviation of 3.4%. In only 3 occurrences is the agreement worse than 10%, and then never greater than 13%. Illuminances from 50 lux to 27,000 lux were accurately predicted under very different sky conditions and for different glazing fixtures.

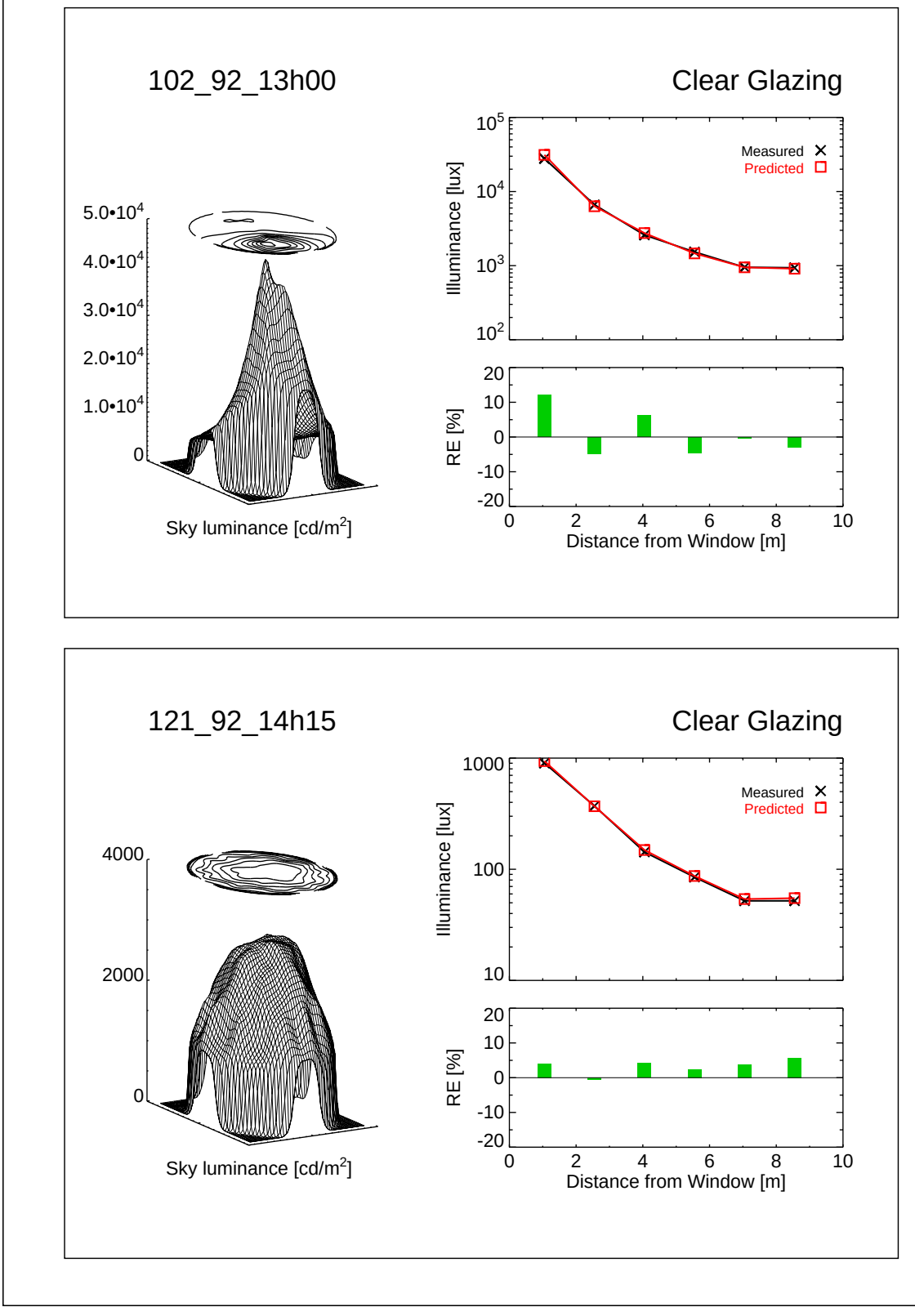

Figure 4-6. Clear glazing - 102_92_13h00 and 121_92_14h15

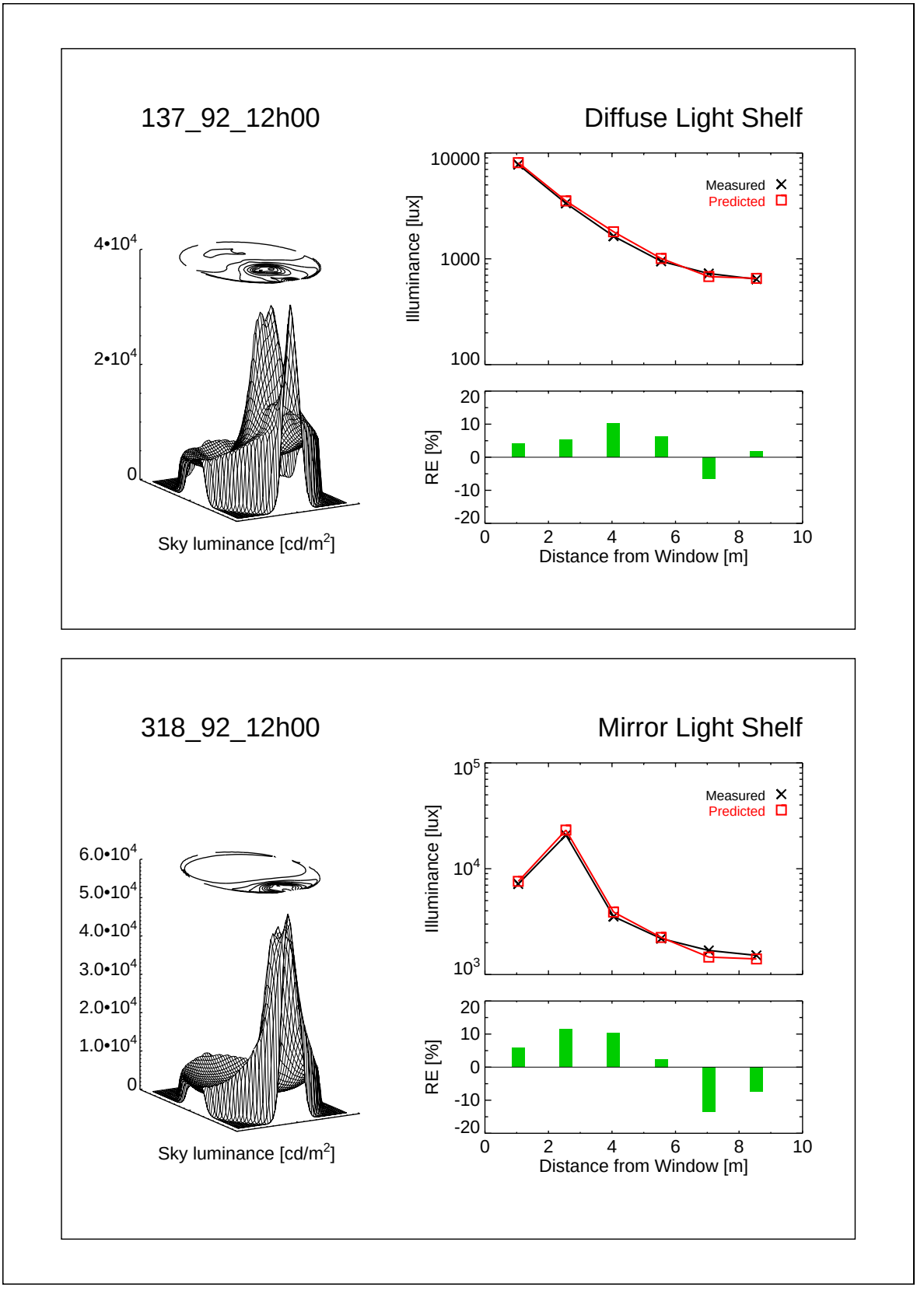

Figure 4-7. Diffuse light shelf - 137_92_12h00 and mirror light shelf - 318_92_12h00

The room illuminance measurements were accurate to within ±5% [Aizlewood 93] and the sky luminance/illuminance data were accurate to within ±10%.[4] Percentage uncertainties in other input parameters, e.g. surface reflectivities, were less than that for the monitoring instruments. For the inter-reflection part of the lighting simulation, random errors are an inherent feature of a Monte-Carlo approach since a limited number of rays are used to sample a continuous luminous environment. Also, systematic under prediction might result from modelling what is effectively an infinite number of reflections with a restricted number of ambient bounces. However, using the basecase set of ambient parameters (Section 3.3.2), these errors were reduced to a negligible level. Compared to the uncertainties associated with the monitored data, the agreement between measurement and prediction for these four cases must be considered to be very good; errors resulting from the simulation model, random or systematic, are not significant compared to the errors in the input parameters. Note that there was an element of luck in the selection of these four cases; errors of the type proposed in Section 3.2.7 (see Table 3-9) were either absent or negligible in effect.

Following the initial specification of an overcast and a sunny sky day for the clear glazing cases, and clear skies for the two light shelf cases, the days were chosen at random. For the clear sky cases, times around noon were selected to ensure that there was solar penetration into the office space. The complex luminance patterns that can result under these conditions are illustrated in Figure 4-8. Here a rendering of the office space with the mirror light shelf at time 318_92_12h00 is shown as a 'normal' image and a false colour luminance map. For this case, the predicted field-of-view luminance ranges from ~500 to 40,000 cd/m^2. The internal illuminance predictions for this case were good (Figure 4-7), so it is reasonable to assume that the predicted field-of-view luminance was correspondingly accurate. These sky conditions were likely to be more demanding of the illuminance calculation

4. Private communication - P. Littlefair, BRE.

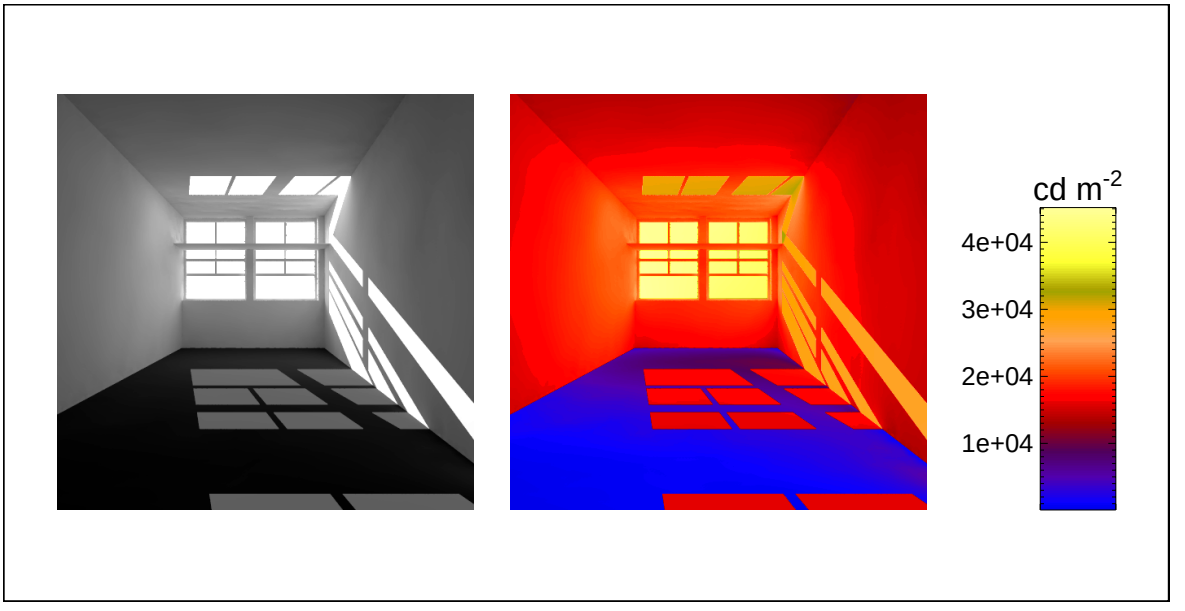

Figure 4-8. Rendering and luminance map for room with mirror light shelf 318_92_12h00

than cases with overcast skies where the luminance range and gradients are generally much smaller.

4.2.2 All 754 skies

Having demonstrated for a test sample that accurate prediction of illuminance was achievable, the next stage was to repeat the simulations for all the 754 skies in the validation dataset. Recall that for the office with innovative glazings, the five different glazing types were cycled throughout the period of monitoring. Furthermore, only two of these - the diffuse and mirror light shelves - could be modelled using 'normal' materials. The ordinary glazing office therefore was exposed to the greatest number of skies; that is, 754. Consequently, this office configuration was used for the all-skies validation. The *Radiance* simulations for this were carried out using the automation procedure described in Section 3.3.4.

The internal illuminance predictions at the six photocell locations for the 754 skies are presented in four groups of summary plots. The first group is a set of six scatter plots of the predicted versus measured illuminances at each photocell, Figure 4-9. The measured internal illuminances range from

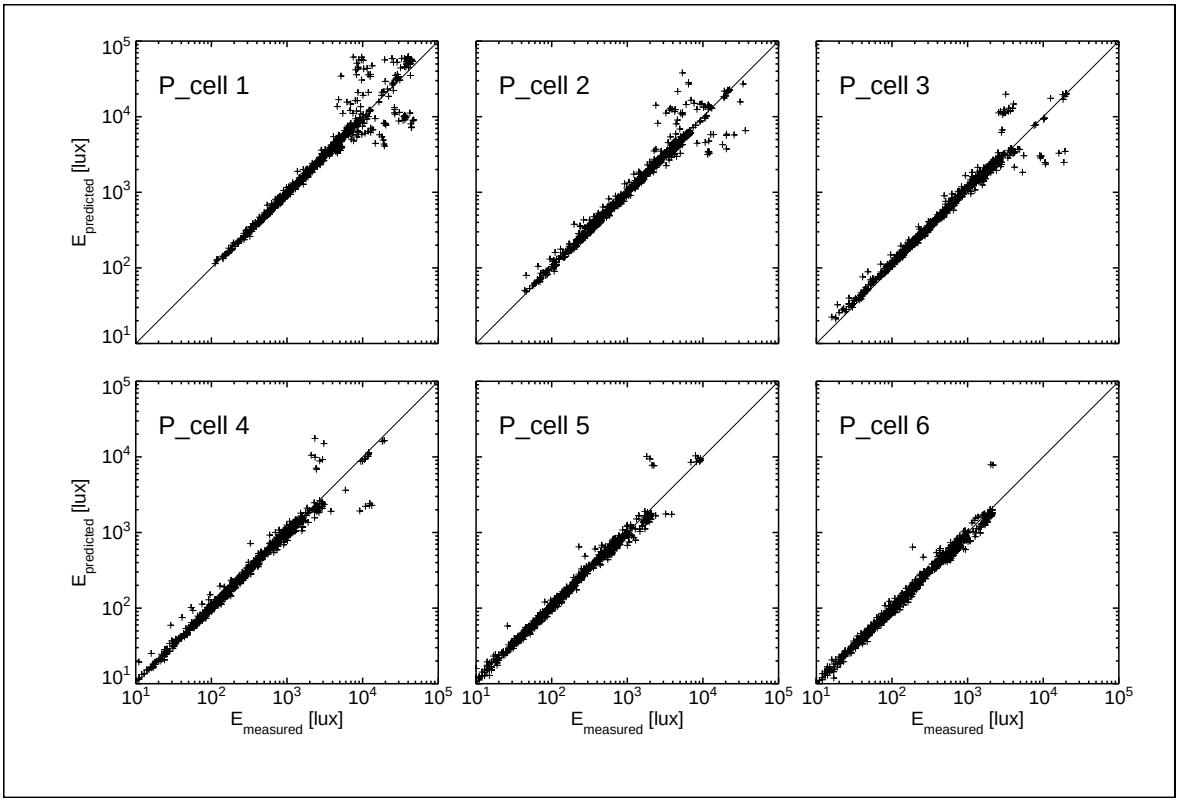

Figure 4-9. Predicted vs measured illuminance scatter plot

~10 lux to ~50,000 lux (logarithmic scaling is used). These plots show that the majority of the predictions were at least reasonably accurate: the points are mostly straddling the equality line. However, it can be seen that inaccurate predictions - both over and under - were more likely at high illuminances. That is, for bright clear sky conditions rather than for dull skies.

The second group of plots shows the distribution in the relative error for the illuminance predictions at each photocell, Figure 4-10. The RERs were aggregated into 5% bins, over the range -102.5% to +102.5% and the distribution was normalized to total = 1. Marked on each histogram is the 0% line (solid) and the ±10% lines (dashed). Each histogram is annotated with the photocell number, the overall mean bias error (MBE) and the root mean square error (RMSE). Each of the distributions, with the exception of p_cell 3, is fairly symmetric about the 0% line, and the main body of the

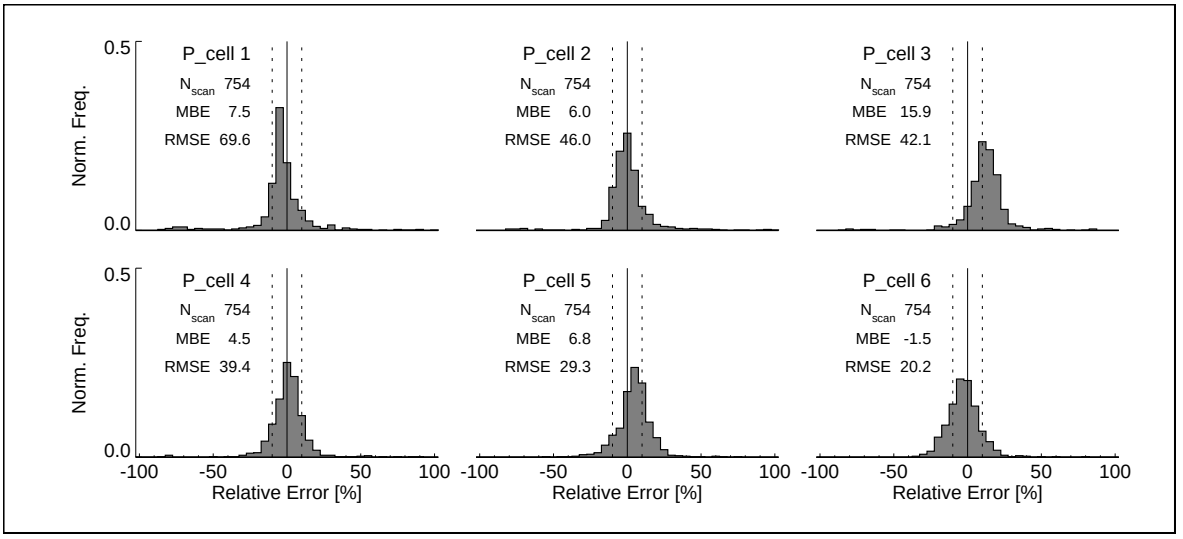

Figure 4-10. Frequency distribution in RER - all skies

distribution is contained within the range ±17.5%. From p_cell 1 at the front of the room to p_cell 6 at the rear, there is a reduction in the kurtosis (or 'peakiness'), of the distribution. High RERs, that is greater than ±50%, occur more frequently nearer the window than at the back of the room - this is revealed in the trend of decreasing RMSE from p_cell 1 to p_cell 6. All the photocells, with the exception of number 6, show a positive mean bias error. This was probably caused by a small number of large over predictions except for p_cell 3 where the main body of the distribution is off-centre with a positive bias.[5]

The third set of plots shows the relative error (RER) in the illuminance predictions versus scan number, Figure 4-11. The RER at each photocell is marked by a black square (■) on a vertical line which indicates the range in the RER at the six photocells for that scan. The RER plot range is limited to ±50%, and RER values outside this range were reset to the nearest range limit, i.e. +50% or -50%. Small downward pointing arrows mark the day boundaries between the scans. For nearly all the scans, there were at least

5. Over prediction can give (positive) RERs > 100%, but the RER limit for under prediction is -100%.

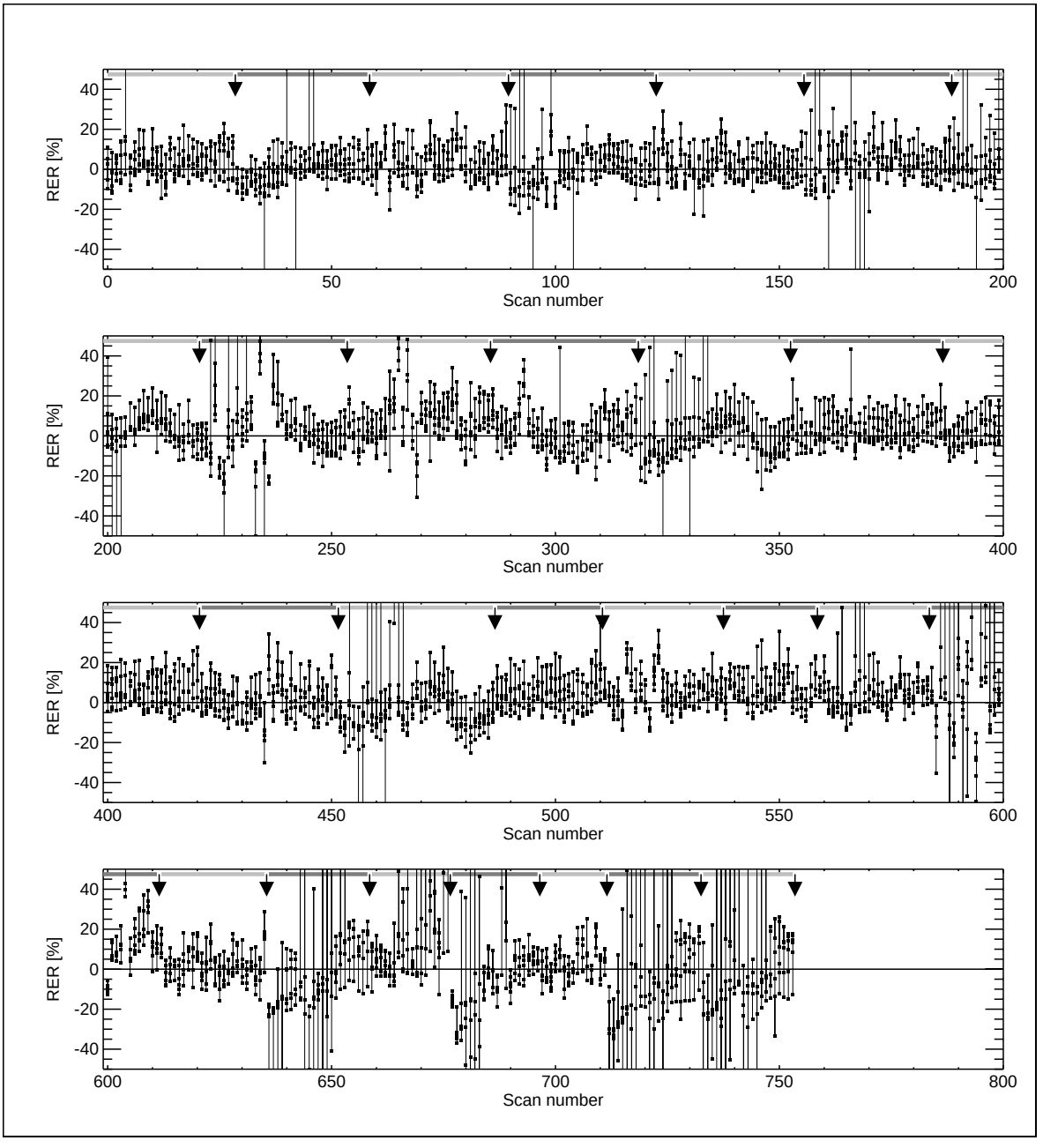

Figure 4-11. Relative error versus scan number

one or two photocell predictions (out of each group of six) that gave a RER within ±10%. The pattern in the RER for the internal illuminance predictions does appear to contain something of the sinusoidal character that was identified in the vertical illuminance predictions (Figure 4-2 - Figure 4-5), also there were conspicuous clusters of high RERs that were

associated with particular days (e.g. scans 712 to 753, days 363 and 364 respectively).

The final plot in this series shows the distribution in the absolute relative error for all the predictions aggregated into 10% bins, Figure 4-12. The last

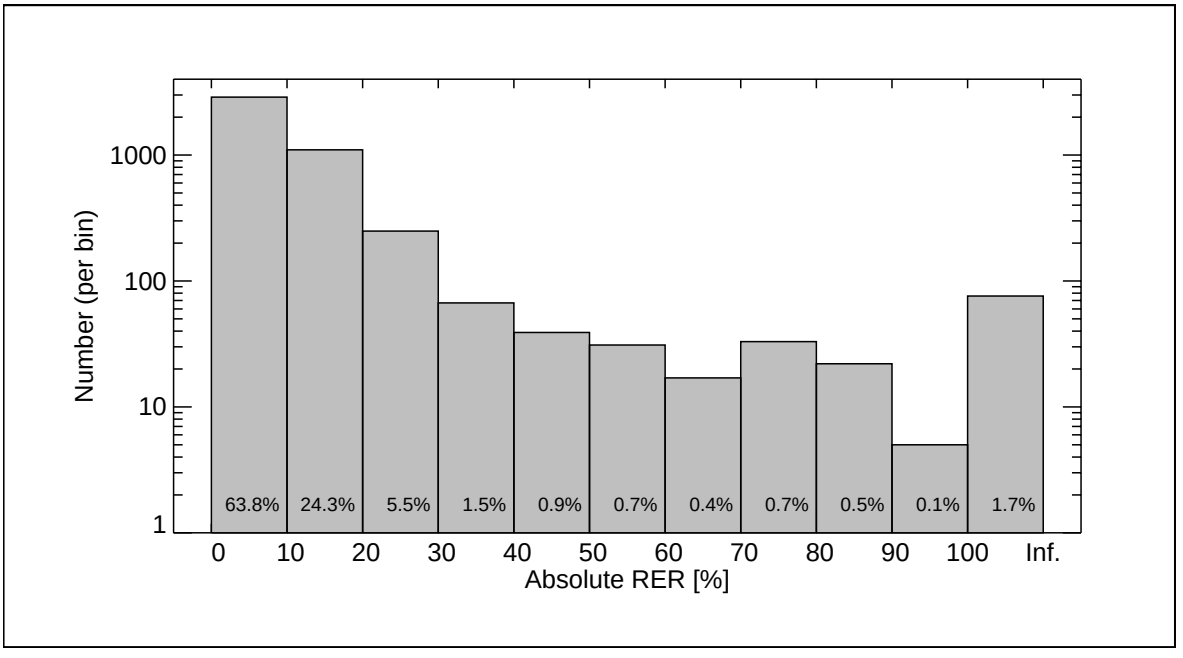

Figure 4-12. Number (per bin) versus |RER|

bin (100 - Inf.) contains all the (absolute) RERs greater than 100%. Each bar of the histogram is annotated with the percentage of the total sample in that bin, e.g. 63.8% of the internal illuminance predictions were within ±10% of the measured value.

The difference in the overall character of the RERs at each photocell suggested that there might be different origins for the cause of the errors. One of the reasons for this suspicion was that there were many occasions when, for a particular scan, the illuminance at the back of the room was accurately calculated and at the front of the room the errors were very large. This finding alone gives reason to suspect that factors other than errors

resulting from the underlying simulation algorithms were present in the results - since the predictions would at first sight appear to be more accurate where the simulation was expending greatest effort.[6]

4.3 Error characteristics related to positional factors

This stage of the analysis examines the relationship between positional factors (e.g. the sun position) and the error characteristics of the illuminance predictions.

4.3.1 Sun angle relative to glazing normal

The first of these examines the relation between the sun angle to the glazing normal and the relative error in the illuminance prediction. For these plots, the angle between the sun and the glazing normal (β) is mapped to a compass rose diagram on which the glazing normal and glazing plane are marked. This mapping gives the opportunity to distinguish between the angles that lie to the east of the glazing normal (β_1) and those that lie to the west of the glazing normal (β_2), Figure 4-13. The magnitude of the RER is given by distance from the origin. A logarithmic scaling was used and circles that encompass the 1%, 10% and 100% RER regions are drawn. At the origin, the RER is 0.1%; RERs smaller than this were plotted here. Separate groups are shown for positive and negative[7] RERs. In the first group, the RER as a function of β is given for each photocell, Figure 4-14. In the second group, the MBE and RMSE are given for the RERs put into bins of angle β that are of size 10˚, Figure 4-15.

Most conspicuous in these two figures is the very low occurrence of negative RERs for p_cell 3. This is consistent with the distribution given in Figure 4-10. It might be expected that a small error in the relative position of the sun and the building orientation could result in significant RERs when, on clear sky days, the sun was near to grazing incidence to the glazing plane. This

6. The illuminance at the back of a room is mainly composed of inter-reflected light which is more difficult to model accurately than direct illumination.

7. For negative RERs, the absolute value is plotted.

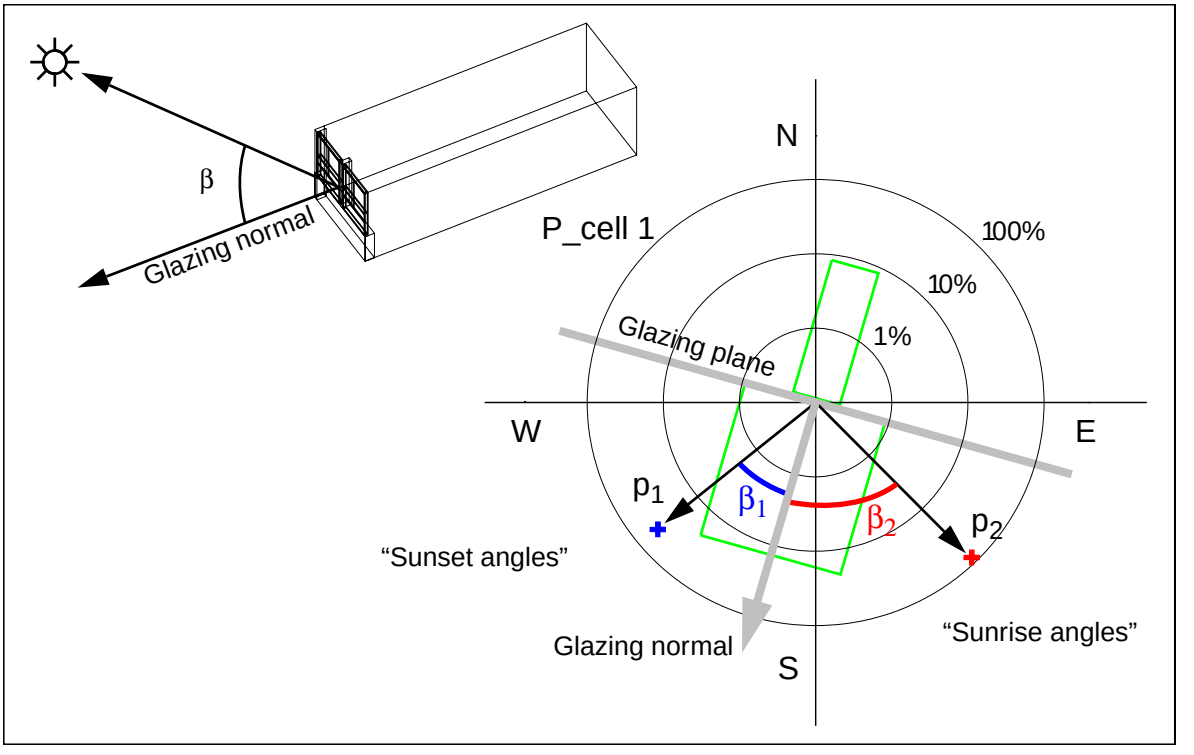

Figure 4-13. Illustration for sun incidence angle plots

does not seem to be the case here: there does not appear to be any significant clustering of high (~100%) RERs when the sun lies near the plane of the glazing ($\beta \cong 90^{\circ}$). The highest (>100%) RERs are all positive and are mostly confined to an arc that is approximately centred on the glazing normal. Furthermore, this arc diminishes in angular extent from p_cell 1 to p_cell 6. This pattern is also apparent in the negative RER plots (close to 100%).

4.3.2 Errors related to the sun angle distribution

Here, the previous analysis is extended and the RERs, now binned, are given in terms of the MBE and the RMSE for each bin as a function of the azimuth and altitude angles of the sun, Figure 4-16. A consistent pattern in the error distribution, i.e. one that persists for all six photocells, could indicate that external structures (or obstructions) significant for light transport were not accounted for in the building model. This does not seem to be the case here, although it should be noted that some of these bins have

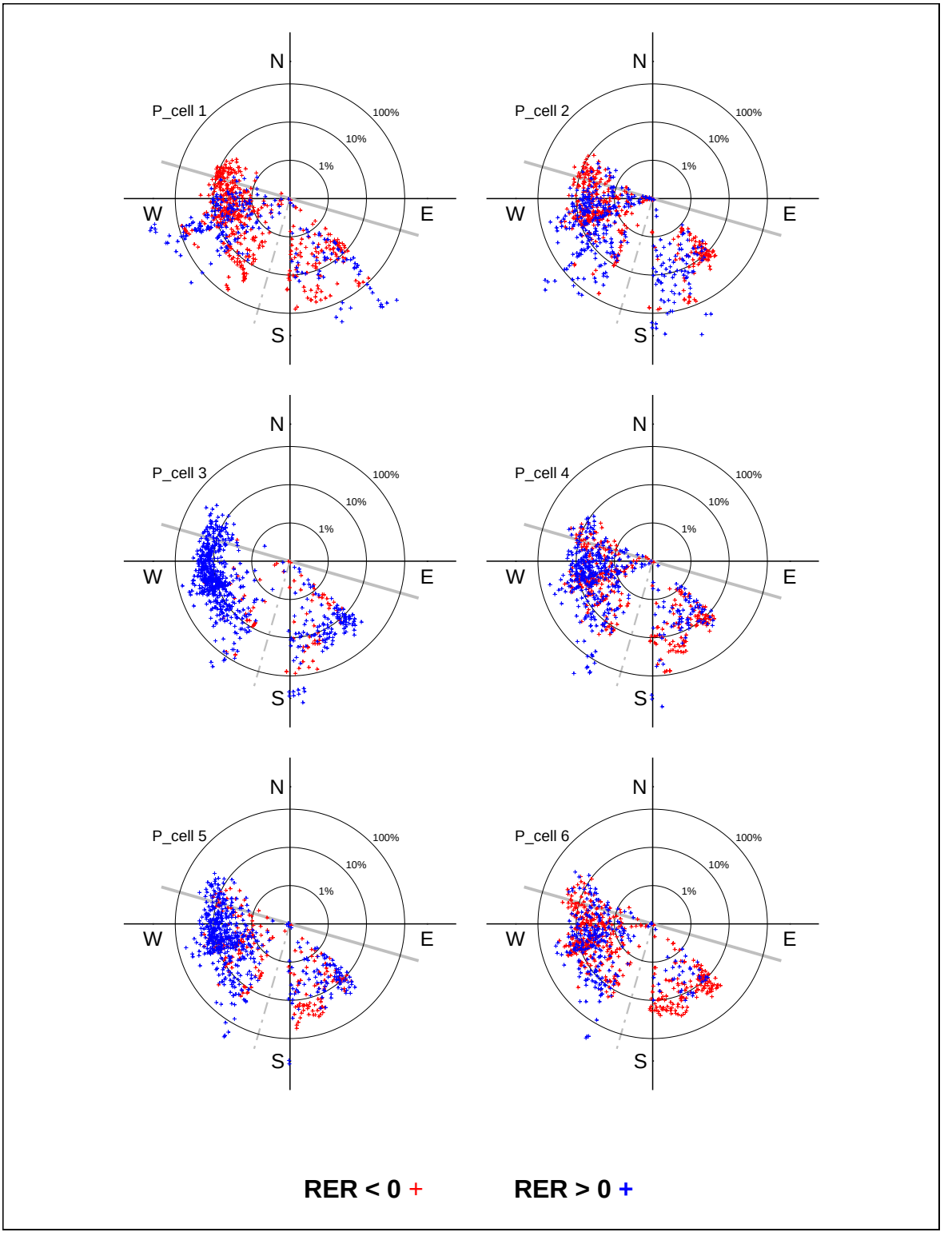

Figure 4-14. Relative error versus angle between sun position and glazing normal

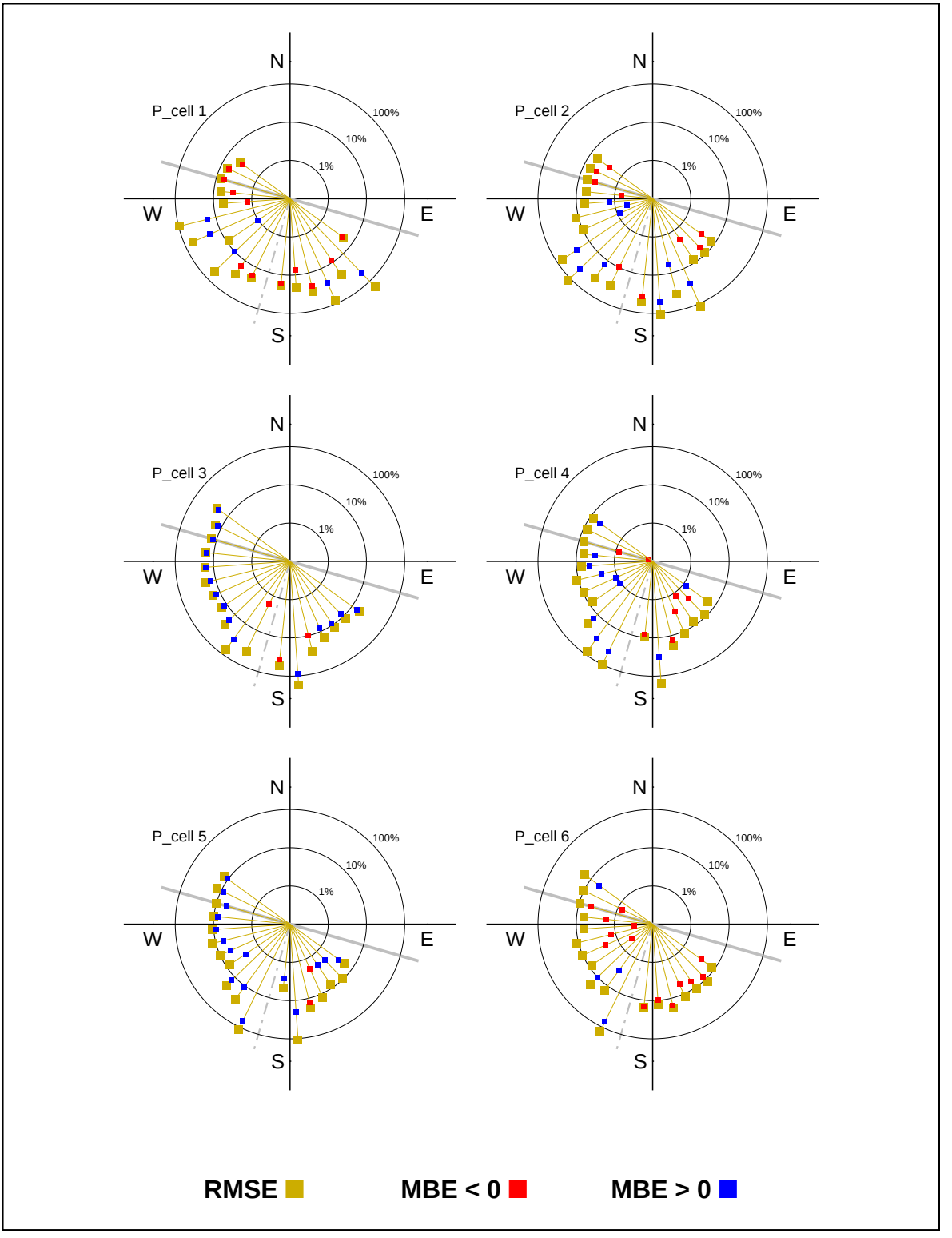

Figure 4-15. Relative error versus angle between sun position and glazing normal

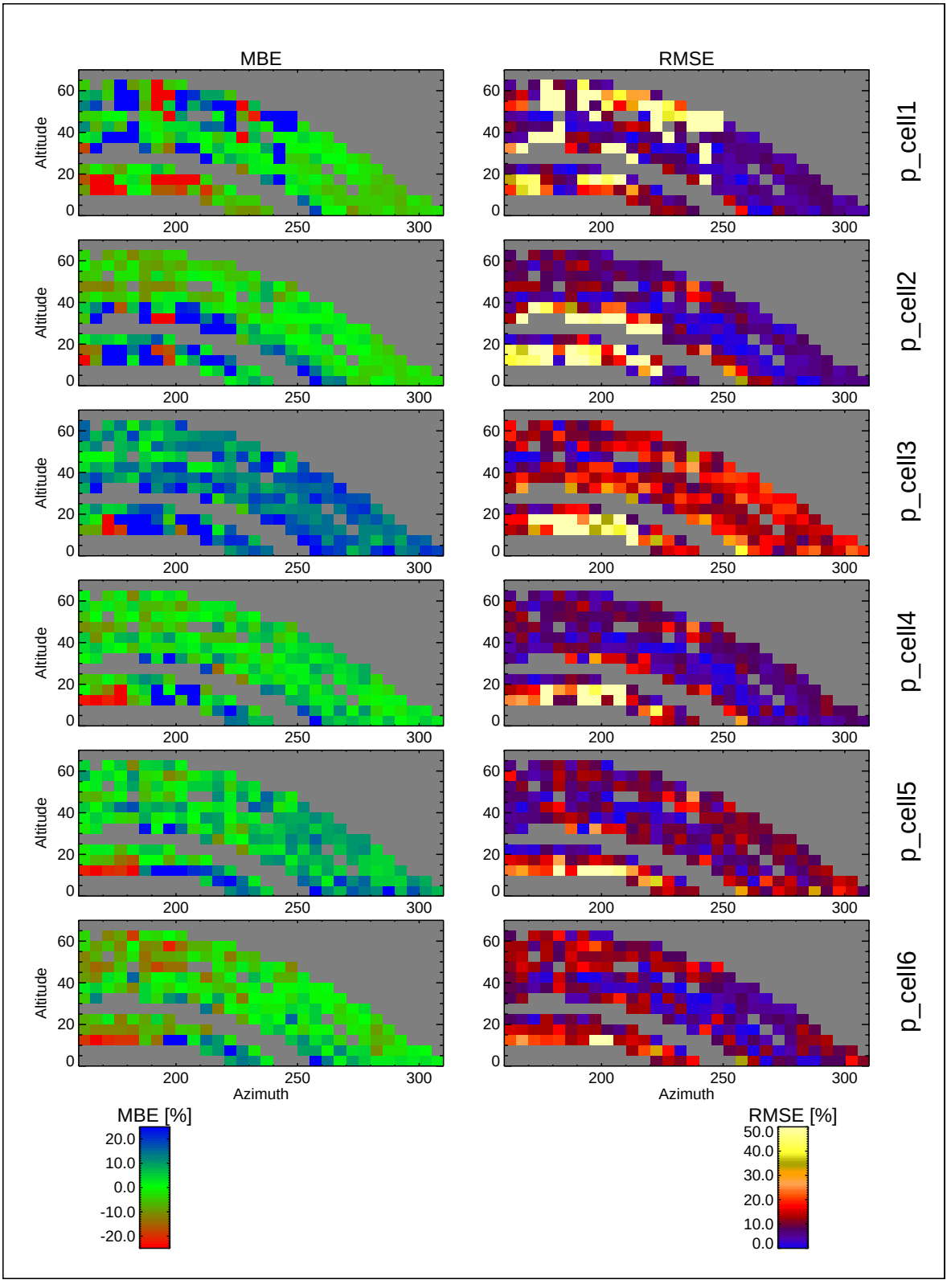

Figure 4-16. MBE and RMSE as a function of binned sun position

very low occupancy. What is clear however is that bins with large RMSEs (> 40%) occur across a wide range of azimuth and altitude values at the front of the office (p_cell 1), and over a very narrow range at the back (p_cell 6). And of course, from p_cell 1 the "view" of the window is much greater than that from p_cell 6. This suggests that the accuracy of the predictions are related in some way to the photocell's "view" of the window. If confirmed, this would lend support to the hypothesis regarding source visibility related errors proposed in Section 3.2.7. In the following section, the relation is examined more closely.

4.3.3 High RERs related to the "view" from the photocell location

In Section 2.6.2 it was shown how renderings "from a light meter's point of view" can be used to understand the luminous environment with regard to illuminance (daylight factor) prediction. That approach was used here to relate the occurrence of high RERs to the photocell "view" of the office. Hemispherical fish-eye view renderings of the office - as seen from each of the photocell locations - were generated using *Radiance*.[8] The sun position for all the predictions where the absolute RER was 50% (i.e. very high) were superposed on each respective rendering (+ mark), Figure 4-17. A label on each rendering gives the number of points plotted, which decreases gradually from 68 at p_cell 1 to only 5 at p_cell 6. Almost all the sun positions are located on the glazing (that is, visible from the photocell), or just off the glazing. As a key, renderings for p_cell 1 and p_cell 6 with all 754 sun positions marked are shown in Figure 4-18. These findings further strengthen the hypothesis that certain sun position - photocell combinations yield unreliable predictions.

8. These renderings were laterally (i.e. East - West) inverted so that, for example, sun positions to the West appear to the left, in keeping with previous figures. Note also that, the hemispherical view for these images contains a cosine weighting of the (hemisphere) projected solid angle. For illumination therefore, equal areas of equal luminance (in the projected view) contribute equally to the total horizontal illuminance at the view point.

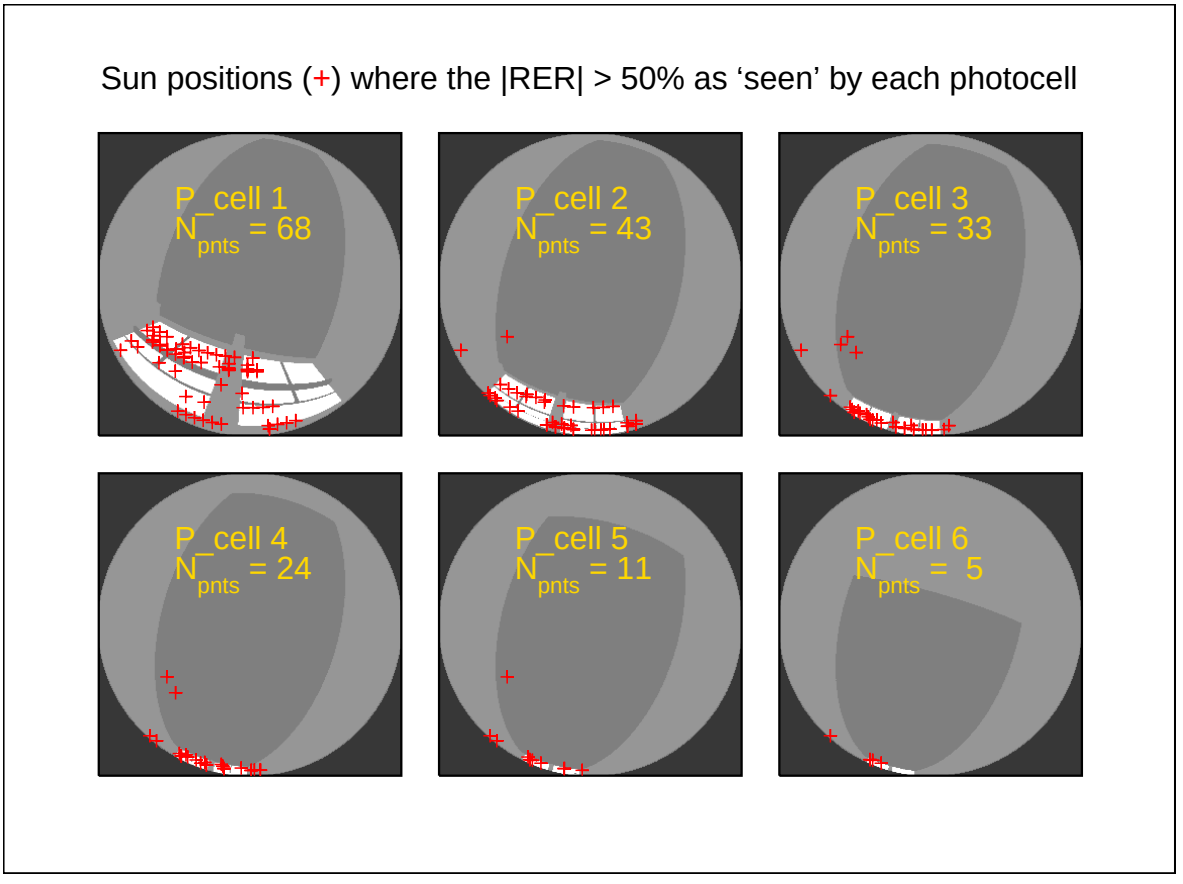

Figure 4-17. Photocell view of sun position

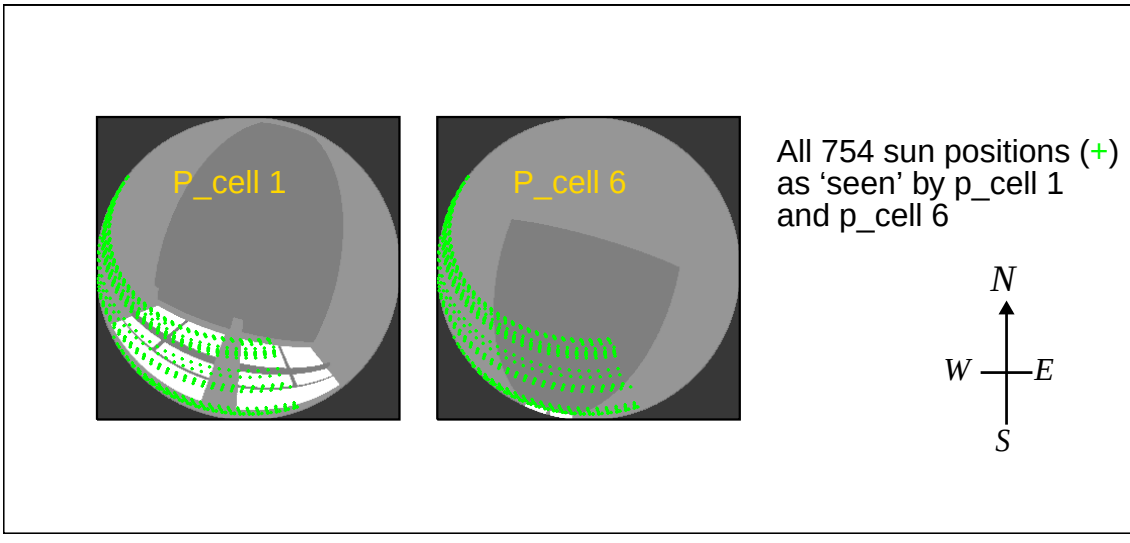

Figure 4-18. Key renderings for sun positions

It could be that significant errors in the illuminance prediction may have resulted from small geometric/orientation differences between the simulation model and reality: since misalignment of just one millimetre can produce large errors when there are shadows cast on - or near to - the photocell by the window frame bars (i.e. Type A errors, Table 3-9). The office glazing had several window bars, and although they were measured individually to an accuracy of ~2mm, positional errors of 1-2cm relative to the overall scale of the room were possible. It was reasonable to assume therefore that at least *some* of the high RERs were due to a mis-match between the modelled geometry and that of the actual office. Given all of the uncertainties, it is virtually impossible to conclusively attribute any one specific high RER to positional misalignment alone. Indeed, the potential for misalignment errors proving significant were largest when the sky was clear, and so shadows were cast by the frame bars. However, these were also exactly the conditions when the uncertainty of the brightness distribution about the solar position could also lead to large errors.

4.3.4 Effect of frame bar shadowing

It was possible to find considerable evidence to support that frame bar shadowing was not the sole cause of large RERs. This was achieved by generating a 'movie' sequence of renderings that showed, for a continuous period in the validation data, the frame bar shadows about the photocell location. The photocells (that is, calculation points) were located at a height of 0.7m above the office floor. Due to projection displacement, the frame bar shadowing on the floor would be very different from that in the (horizontal) plane of the photocell. To make the shadows in the plane of the photocell visible, a white disc (radius 0.1m) was added to the simulation model scene description at each of the photocell locations. A black sphere (radius 0.01m) was added at the centre of the disc to mark the photocell location. The images were generated for a viewpoint at a height of 2m (from the floor) directly above the photocell. An image from one of the generated sequences is shown in Figure 4-19. The labels indicate the dimensions of the disc and

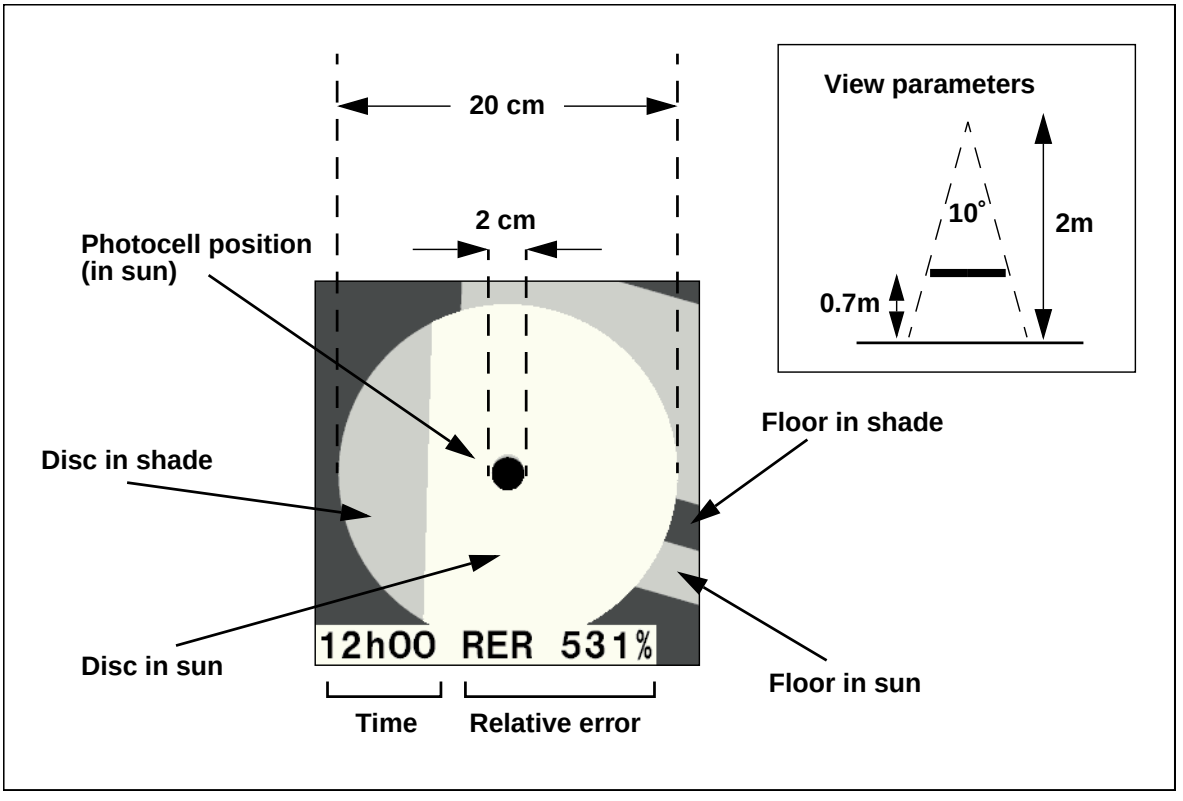

Figure 4-19. Illustration for photocell renderings (127_92_12h00 p_cell 2)

the marker sphere, and the regions of the scene that were (predicted to be) in sun or shade. Each rendering has a label that shows the 'time stamp' and the relative error in the illuminance prediction. Image sequences were generated for three continuous periods of clear sky conditions: photocell 1 for day 102_92 (Figure 4-20); photocell 2 for day 127_92 (Figure 4-21); and photocell 2 for day 318_92 (Figure 4-22).

The first of these image sequences (Figure 4-20) clearly shows the traverse of frame bar shadows across the photocell. Note that, for some of these times, the RERs were very large i.e. > 50% (dashed-line box). It is quite plausible therefore that misalignment was the cause of high RERs for some instances. The other two image sequences (Figure 4-21 and Figure 4-22) also show occasions where a frame bar shadow was (predicted to be) near to the photocell position. Note here however that there does not appear to be a consistent pattern in the relationship between frame bar shadowing

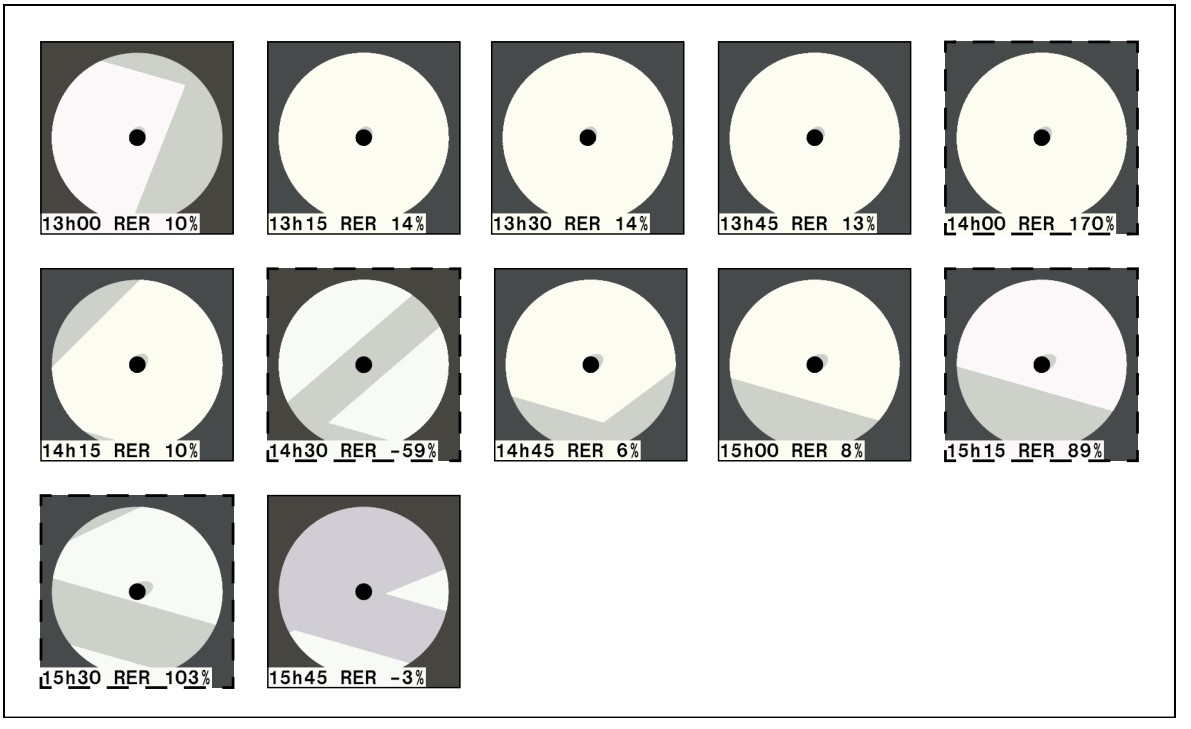

Figure 4-20. Photocell 1 - day 102_92

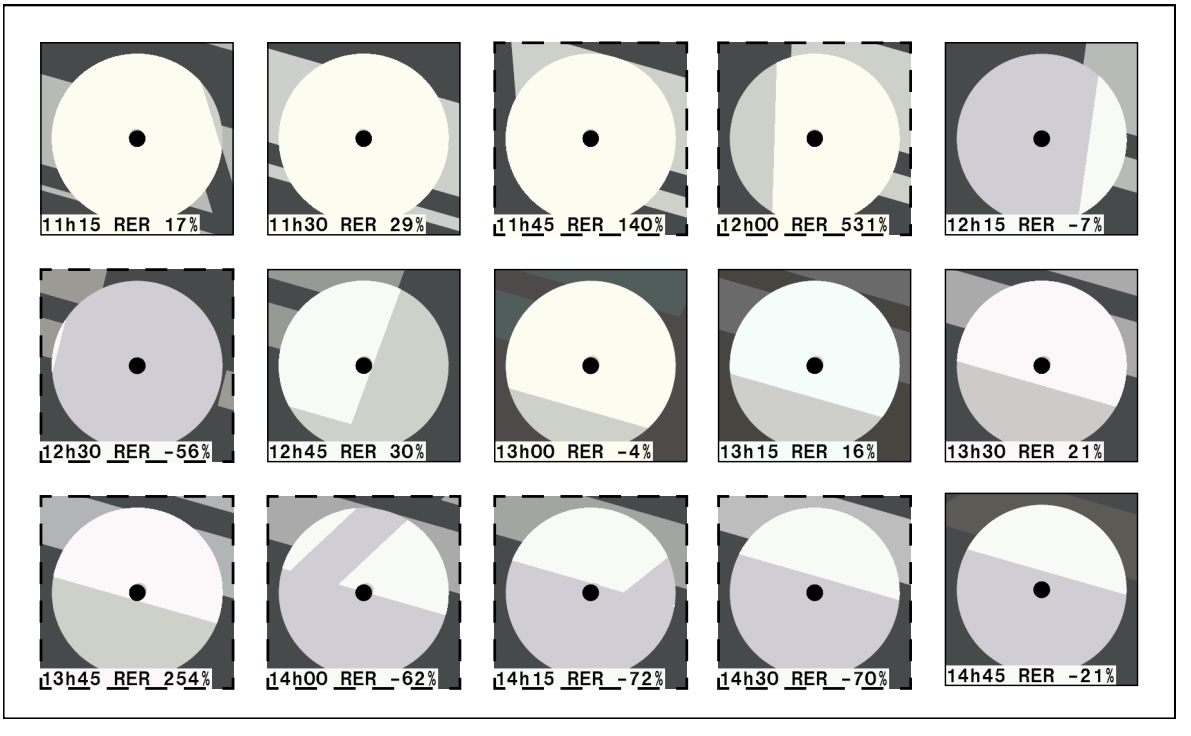

Figure 4-21. Photocell 2 - day 127_92

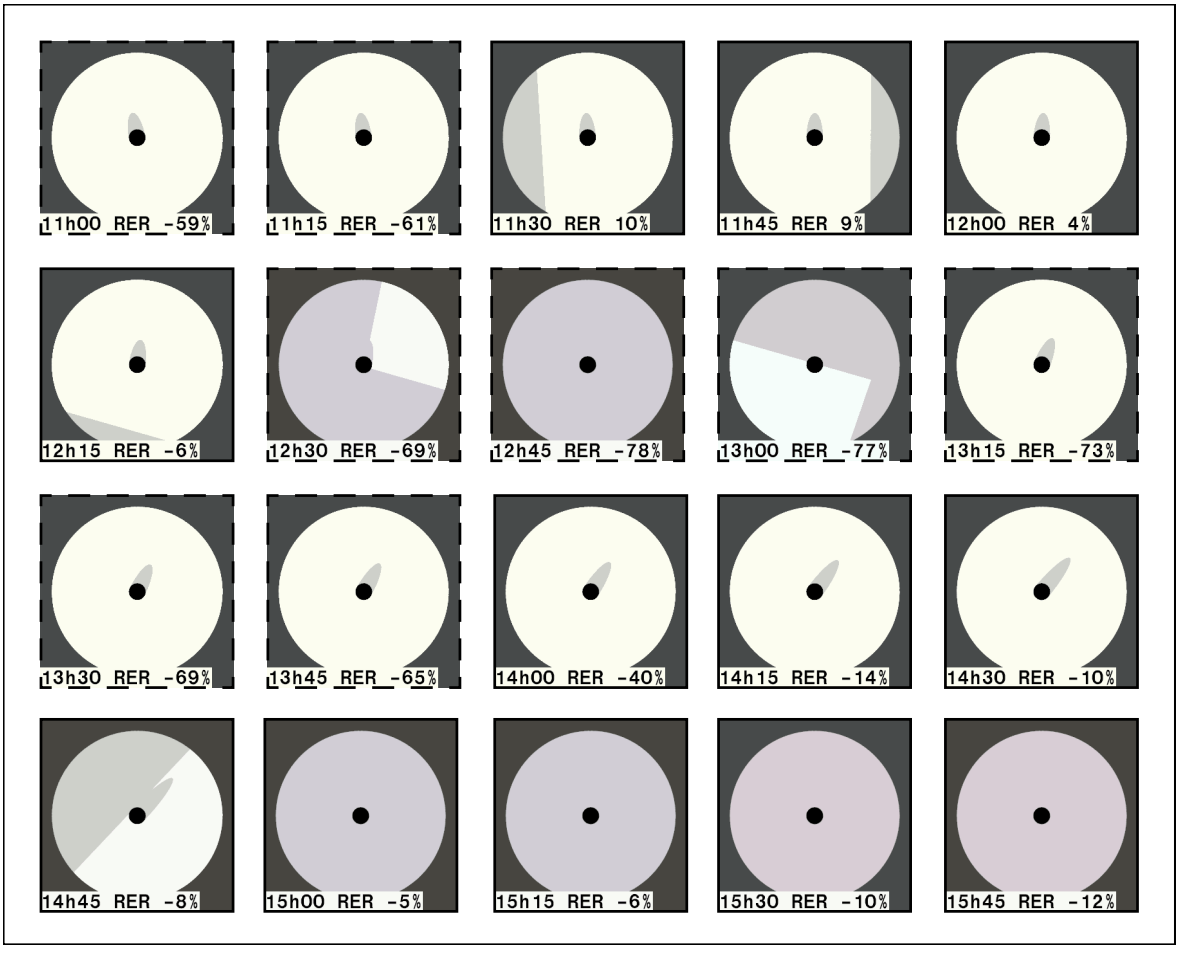

Figure 4-22. Photocell 2 - day 318_92

and the RER for the illuminance prediction. There were several instances where the white disc was either fully in shade or fully in sun, and yet the RERs for these occasions were nevertheless very large (e.g. 11h15 and 12h45 in Figure 4-22). It is unlikely that the magnitude of the geometric mis-alignments would be sufficiently large such that the images would show the white disc fully in shade when an actual disc would have been fully in sun - or vice versa. This suggests that geometric mis-alignment alone is insufficient to explain many of the occurrences of high RERs.

The likelihood that a shadow from a glazing frame bar has traversed the disc in the 15 minute interval between the frames can be roughly estimated as follows. Taking the window mid-point (M) as the “fulcrum”, the horizontal

(Φ_h) and vertical (Φ_v) angles subtended by a shadow-disc at M can be easily calculated from the vector geometry illustrated in Figure 4-23. The

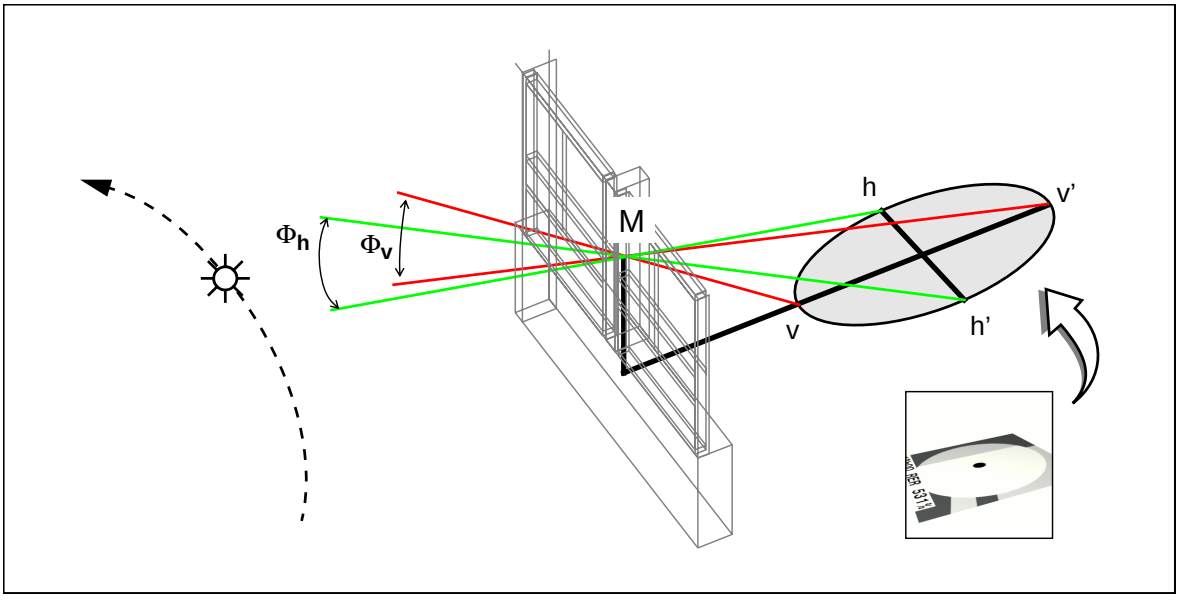

Figure 4-23. Vector geometry

horizontal and vertical angles subtended by the shadow-disc at all six photocell locations are given in Table 4-3. Also given is the equivalent

P_cell	Horizontal displacement		Vertical displacement	
	Angle Φ_h [°]	t_{equiv} [mins]	Angle Φ_v [°]	t_{equiv} [mins]
1	8.7	34.7	5.3	21.1
2	4.3	17.1	1.3	5.1
3	2.8	11.1	0.5	2.2
4	2.0	8.2	0.3	1.2
5	1.6	6.5	0.2	0.7
6	1.3	5.3	0.1	0.5

Table 4-3. Approximate horizontal and vertical angles subtended by shadow discs at glazing mid-point

transit time of the sun - moving at 15° hour^{-1} - to traverse the angles.[9] For times around midday when the sun is about its zenith, the sun's angular

motion is largely composed of a change in azimuth angle, i.e. horizontal. At these times, the change in altitude (i.e. vertical angle) is relatively small and, for the purpose of this illustration, can be ignored. In which case, the approximate time needed for a shadow of the window mid-point (i.e. frame bar) to traverse the shadow-disc is ~35 mins for p_cell 1 and ~17 mins for p_cell 2. For example, the (largely horizontal) transition of a frame-shadow is captured in images 14h15 to 14h45 (Figure 4-20). A transition time of ~30 mins is indicated which is consistent with the value given in Table 4-3. It can be fairly confidently asserted therefore that, for the sequences given in Figure 4-20 and Figure 4-21, the traversal of all the frame-bar shadows has been captured in the images. Additional tests using a lower position for M (more realistic for low-altitude winter sun) indicate that this was the case for the sequence in Figure 4-22 also.

4.4 Errors related to illuminance components

It was shown in Section 4.3.3 that the majority of the high (> 50%) RER predictions occurred when the sun, and therefore the circumsolar region, was visible from the photocell location. It might also be possible to associate these high error cases with the relative contributions that the components of illuminance (direct sky etc.) made to the total illuminance. If established, a relation could serve to identify “at risk” cases in the validation data. Note that, although a strong *relation* between circumsolar visibility and inaccurate predictions is clearly present in Figure 4-17, the inaccurate predictions were selected *a priori* and superpositioned over the renderings. That, in itself, does not constitute a test. For the tests described below, the relations examined were between the error in prediction and:

- the fraction of the (predicted) illuminance from inter-reflected light only; and,
- the fraction of the (predicted) illuminance due to the direct sky component.

9. The vertical angle is, of course, hypothetical.

4.4.1 Components of illuminance

With *Radiance* it is a relatively straightforward task to manipulate the scene description and/or the calculation parameters to determine, in one or more steps, any conceivable component of illuminance, e.g. externally reflected light from the sky only. For the purpose of these tests, the total predicted illuminance (E_p) can be taken to be the sum of three distinct illuminance components: the direct sun illuminance (E_{sun}), the direct sky illuminance (E_{sky}) and the illuminance due to inter-reflection (E_{int}), e.g.

$$E_p = E_{sun} + E_{sky} + E_{int}$$

The last component is all the light that arrives at the calculation point following one or more reflections, from either internal or external surfaces, Figure 4-24. For any given sun and sky description, the direct sun and

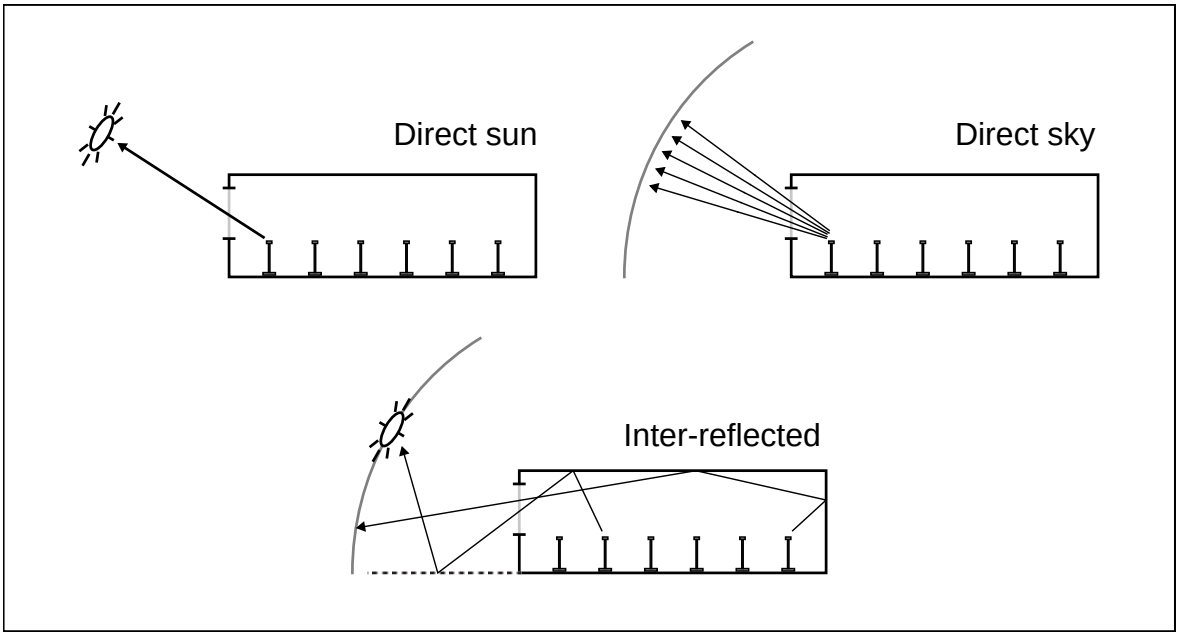

Figure 4-24. Illuminance components

direct sky components can be evaluated with relative ease and certainty. That is, certainty with respect to the *model* description. The simulation of inter-reflected light is considerably more demanding, and, so one might

expect, this is where the potential for errors are greatest. To test this, the relation between the relative proportions of the predicted components of illuminance and the RER were examined.

In the first instance, it was the total illuminance at each photocell that was predicted. The proportion of the total (predicted) illuminance that was due to (a) the sky component, and (b) the direct sun component could thereafter be computed fairly rapidly since neither case required a (recursive) inter-reflection calculation. The illuminance predictions for all 754 were re-computed[10] - with the inter-reflection calculation switched off - for the office model with:

1. a model sun description only; and,
2. a model sky description only.

The sum of the two components subtracted from the total predicted illuminance yielded the (predicted) illuminance that was due to inter-reflected light only:

$$E_{int} = E_{tot} - (E_{sun} + E_{sky})$$

The sky was visible through the glazing from all photocell locations so each photocell received some direct sky illuminance, but only occasionally did a photocell receive direct sun light. All photocells received, of course, inter-reflected light.

4.4.2 Errors versus fraction of illuminance component

In order to make comparison between cases, the absolute fractional error (AFE) in the illuminance prediction, $|(E_p - E_m)|/E_m$, was plotted against the magnitude of the predicted illuminance component expressed as a fraction of the total predicted illuminance. This was done (for each photocell) for the inter-reflected component E_{int} (Figure 4-25) and for the sky component E_{sky}

10. The simulations were carried out using the automation scheme described in Figure 3-31 on page 95.

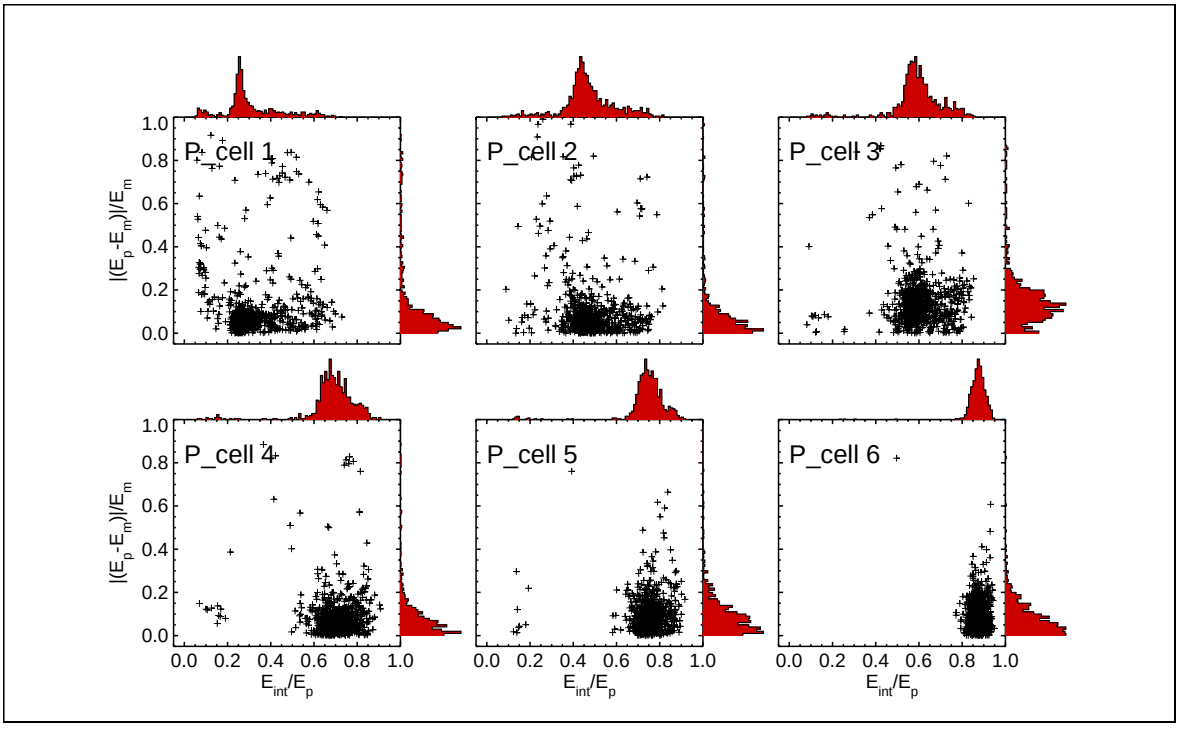

Figure 4-25. Fraction inter-reflected component by photocell

(Figure 4-26). The number distribution of the points along the ordinate and abscissa axes was plotted on the top and right-hand edge of each plot (a bin size of 0.01 was used).

Looking first at the inter-reflected component, the difference in the scatter of the points between the photocells is most obviously apparent. At the back of the room (p_cell 6), the points are mostly clustered in the range E_{int}/E_p = 0.8 to 0.95, and for this cluster the AFE was fairly low - most of the points were in the range AFE = 0 to 0.2 (i.e. relative errors in the range ±20%). Turning now to the absolute fractional error for inter-reflected light - points and distribution - at p_cell 1, there were large errors across the range of E_{int}/E_p. In contrast, at p_cell 6 there were only a few instances where the AFE was greater than 0.3. Since there were only relatively few instances where a photocell received some direct sun light, the E_{sky}/E_p plots for the sky component appear similar to a lateral inversion of the inter-reflected component plots.

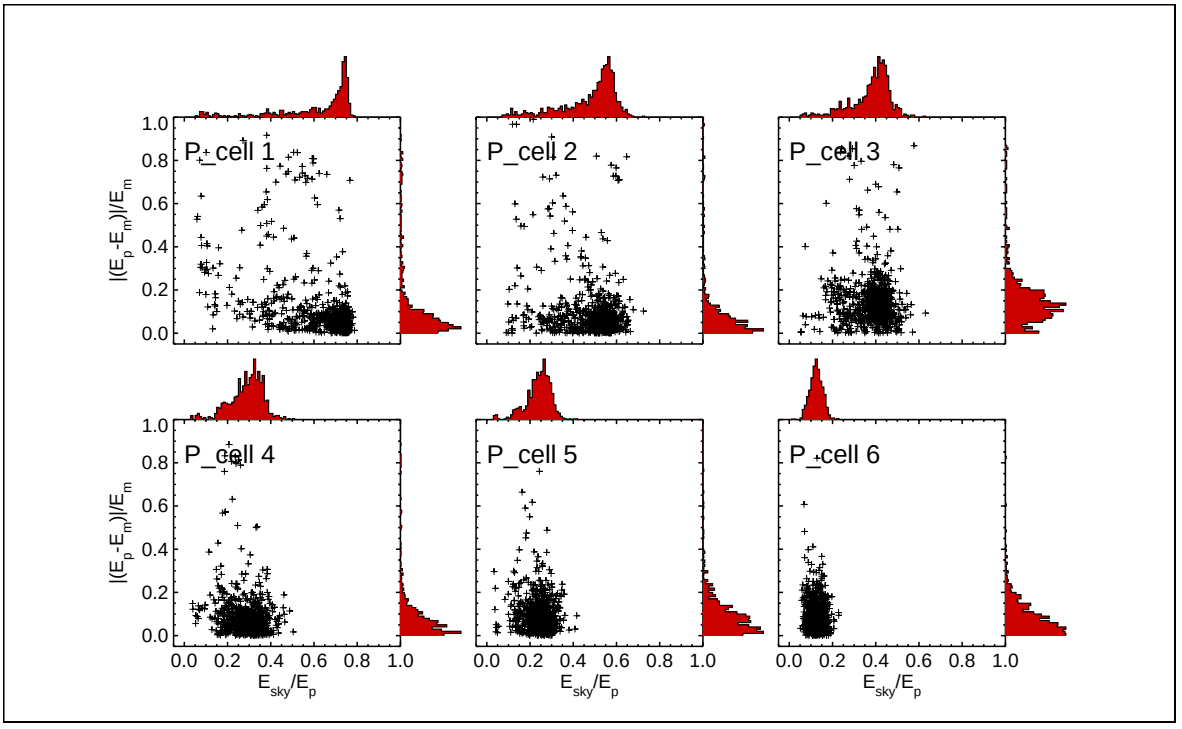

Figure 4-26. Fraction sky component by photocell

For Figure 4-27, the AFE data shown in Figure 4-25 & Figure 4-26 have been aggregated into bins of width 0.1 for each of the fractional components, and the mean absolute fractional error (MAFE) for the predictions in each bin are shown as a histogram. The bold vertical line on each of the histogram bars indicates one standard deviation from the MAFE. Below each of the MAFE component histograms for E_{int}/E_p and E_{sky}/E_p is a plot showing the number of points in each of the bins. Because each photocell prediction was considered individually, there were 754 x 6 = 4524 predictions in total. For low fractions of the inter-reflected component (0 to 0.2), the MAFE was large, as was the scatter in the predictions. This range accounts for only a relatively small number of predictions from the entire sample. For $E_{int}/E_p > 0.2$, the MAFE drops sharply to ~0.1 and remains fairly steady, but the standard deviation gradually diminishes with increasing E_{int}/E_p. The range $0.6 \leq E_{int}/E_p \leq 0.9$ account for over half of all the predictions. The MAFE as a function of (binned) E_{sky}/E_p shows a similar

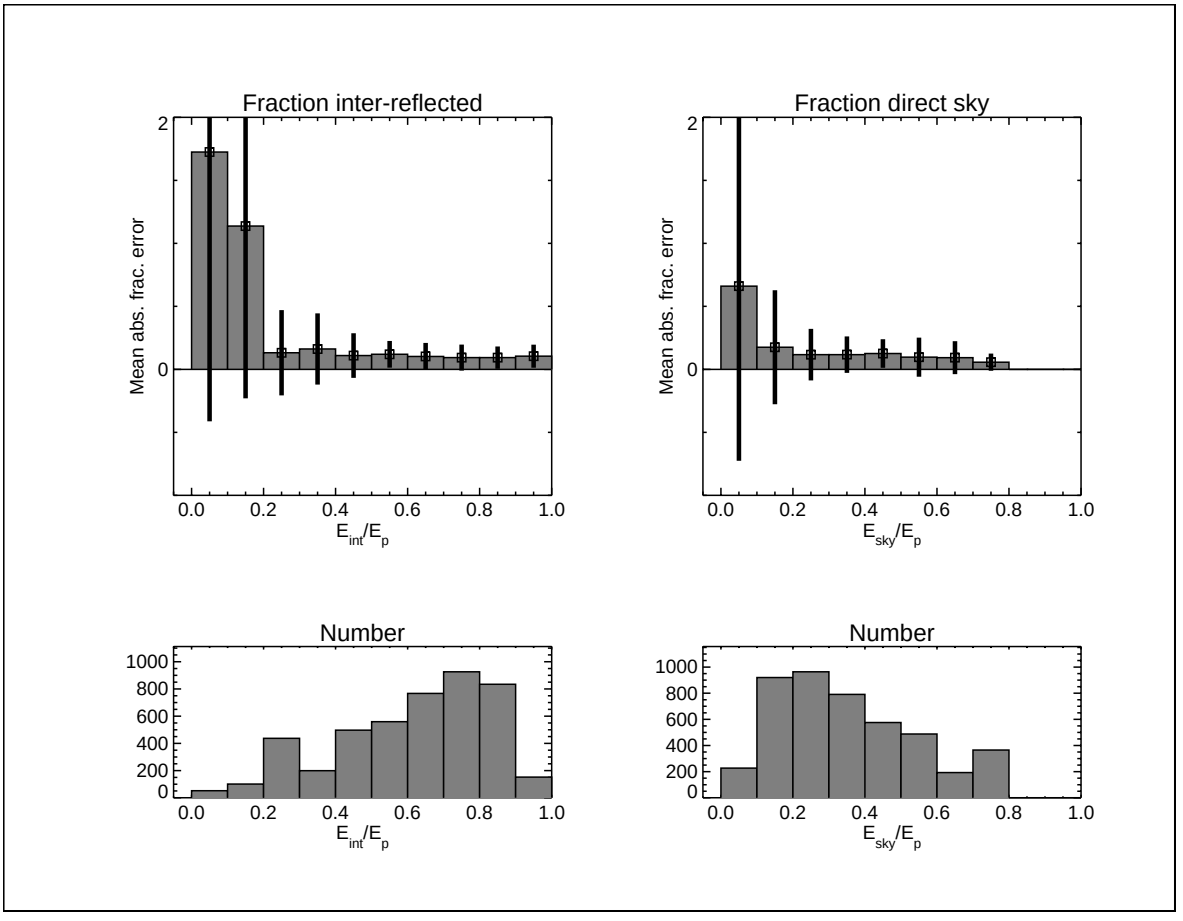

Figure 4-27. Mean absolute fractional error as a function of binned fractional component of illuminance

trend to that for E_{int}/E_p, only here the peak of the number distribution is in the range $0.1 \leq E_{sky}/E_p \leq 0.4$.

From either of these plots it is possible to determine a discriminator that could be used to partition the photocell-sky combinations so that one population contained mostly accurate predictions. For example, predictions where either $E_{int}/E_p \geq 0.4$ or where $E_{sky}/E_p \geq 0.3$ would function as fairly robust discriminators. There are shortcomings however in using either of these ratios as discriminators for filtering out un-reliable predictions. Firstly, a mechanism has not yet been proposed that might explain the relation. And secondly, the application of either discriminator may unduly bias the validation sample to a limited range of sky types - thus

compromising the generality of the validation. Using $E_{sky}/E_p \geq 0.3$ does indeed bias the sample to predominantly overcast skies, whereas applying $E_{int}/E_p \geq 0.4$ preserves a wider range of sky conditions and rejects fewer cases from the total number of photocell-sky combinations. This is shown in Figure 4-28 where the effect of applying the discriminator on the sky type is shown. For example, applying $E_{int}/E_p \geq 0.4$ removes less than 0.2 (i.e.

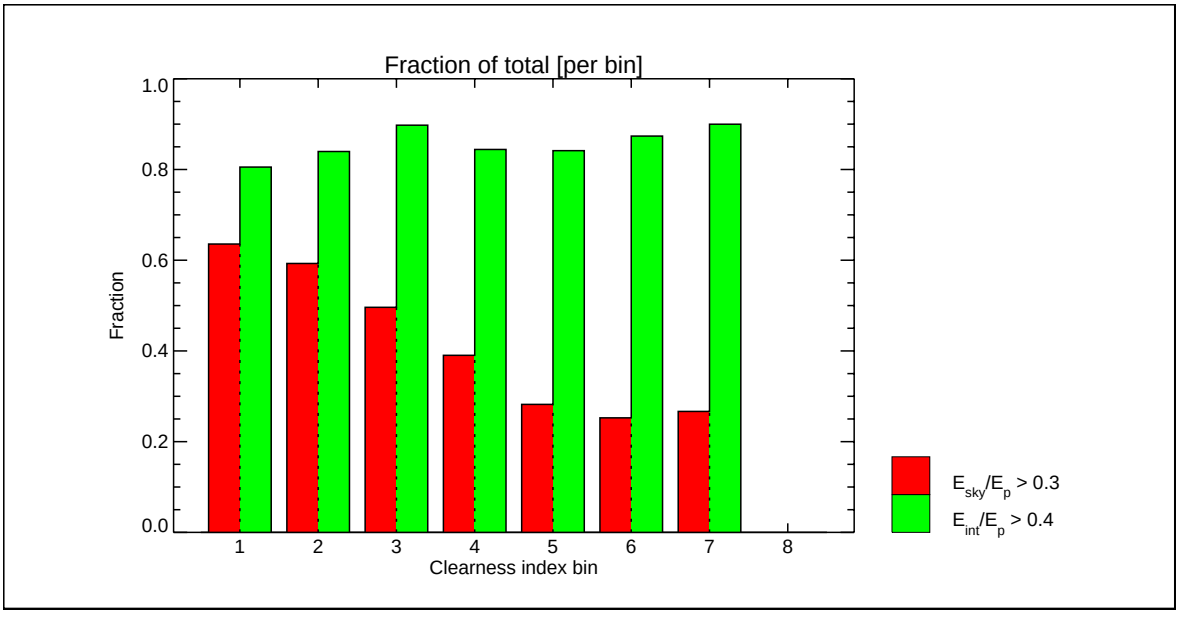

Figure 4-28. Fraction of total per bin

20%) of the skies from any of the sky clearness index bins. Whereas, using $E_{sky}/E_p \geq 0.3$ removes from the sample more than half of skies with a clearness index bin greater than 3.

4.4.3 Summary

To summarise the findings discussed above:

1. Skies where $E_{int}/E_p \geq 0.4$ are associated with accurate (MAFE < 0.2) illuminance predictions. These cases make up ~82% of the total sample and they cover a wide range of sky conditions.

2. Skies where $E_{sky}/E_p \geq 0.3$ are also associated with accurate illuminance predictions. These cases make up ~53% of the total sample, but the clear sky conditions are under-represented in preference to overcast sky conditions.

In other words, illuminance predictions with a significant inter-reflected component ($E_{int}/E_p \geq 0.4$) tended to be accurate regardless of the sky type. Whereas, illuminance predictions with a significant direct-sky component ($E_{sky}/E_p \geq 0.3$) tended to be accurate mainly for overcast conditions.

4.5 Partition of the validation dataset

The findings described in the previous sections are summarized as follows:

1. For the majority of cases (2885, or 64% of the total), the internal illuminance was predicted to a high degree of accuracy (±10%).
2. There were a small number (184, or 4% of the total) of conspicuously inaccurate predictions where the |RER| > 50%. However, it was rarely the case that, for any one sky, the accuracy was this poor for all six photocells.
3. The high RER predictions were strongly associated with visibility (total or partial) of the circumsolar region from the photocell location.
4. Positional/geometric errors in the model description were unlikely to be the sole cause of most of the high RER predictions.
5. Accurate predictions, for all sky types, were associated with a significant (predicted) component of inter-reflected illuminance, i.e. $E_{int}/E_p \geq 0.4$.

Taken together, these findings support the hypothesis given in Section 3.2.7 that there exists in the validation dataset a class of errors that are related to imprecision in the model geometry and/or the sky description. That hypothesis is tested by partitioning each of the illuminance predictions using visibility of the circumsolar region as the discriminator. Predictions

for those photocells that did not 'see' the circumsolar region are then compared with the predictions for those that did 'see' the circumsolar region. The test and the results using the partitioned illuminance predictions are described below.

4.5.1 Test for circumsolar region visibility

The extent of the circumsolar region for the test should be large enough to reduce, or possibly eliminate, all four types of source visibility related errors outlined in Table 3-9. Referred to here as the circumsolar exclusion region (CER), it should not be made too large so that many predictions (that is, photocell-sky combinations) are excluded un-necessarily. The largest luminance gradients around the circumsolar region will be for clear skies at the transition between the sky and the (0.5˚) solar disc. Recall that the average luminance across a 6˚ circumsolar region was measured (indirectly) by the solar tracker. It is not possible to disaggregate with any certainty the sun luminance (magnitude) from the sky luminance (magnitude and distribution) within this region. Around the 6˚ circumsolar region, the sky luminance was estimated using interpolation. The full extent of uncertainty in the sun and sky luminance therefore covers a region that is at least 11˚ across.[11] The sky luminance gradients in this larger region however are likely to be much smaller than those within the 6˚ disc. For this reason, the angular extent of the CER was chosen to be, in the first instance, 6˚. The visibility test for the CER was carried out for each of the 4,524 photocell-sky combinations in the validation dataset. This was achieved by using, for each of the 754 skies, a 6˚ unit-brightness 'sun' centred on the sun position. The 6˚ 'sun' (that is, the CER) was the only luminous source in the model. To test for visibility of the CER, a ray bundle was aimed at the CER from each of the six photocells. A description of the generation and aiming of the ray bundle follows.

11. There were occasions when more than one scanner measurement around the solar position was "out-of-range".

For a disc, centre (0,1,0), normal (0,1,0) which subtends an angle of 6˚ at the origin, the (x,z) co-ordinates of ~1000 points randomly distributed across the disc were generated. The (x,y,z) co-ordinates of the origin and these points gave normalized direction vectors. These vectors formed the basic ray bundle for visibility testing. To test for visibility of the CER, a scene description of the office model with the CER at the sun position was generated. The transformation of the bundle centre (i.e. unit vector [0,1,0]) to the sun position was applied to all the vectors in the ray bundle. The vector list for the ray bundle was then replicated 6 fold, and the co-ordinates of the photocells were added to the list. Thus, a list of ray origin and direction vectors was formed for use with the **rtrace** program, Figure 4-29. If, from one photocell, all the rays aimed towards the CER returned zero luminance, then from that photocell, the CER was not visible. If however, one or more of the rays returned a non-zero luminance, the CER was visible, and the degree of visibility was calculated from the number of non-zero luminance rays. The CER visibility was determined for each of the 754 unique sun positions in the validation dataset. Once again, this test was carried out using the automation scheme described in Figure 3-31.

4.5.2 Results for the partitioned data

The illuminance predictions at each of the six photocells for the 754 skies were partitioned into sets designated as either ‘reliable’ or ‘potentially unreliable’ depending on the visibility of the circumsolar region from each of the photocell positions. The RERs for the ‘reliable’ and the ‘potentially unreliable’ sets were aggregated into frequency distribution histograms. The RER bin size was 5% and the number in each distribution was normalised. Each histogram is annotated with the photocell number, the number of predictions in the sample, the overall mean bias error (MBE) and the root mean square error (RMSE).

Considering first the predictions from the ‘reliable’ photocell-scan combinations, i.e. where the CER was not visible (CS6-VIS) Figure 4-30(a).

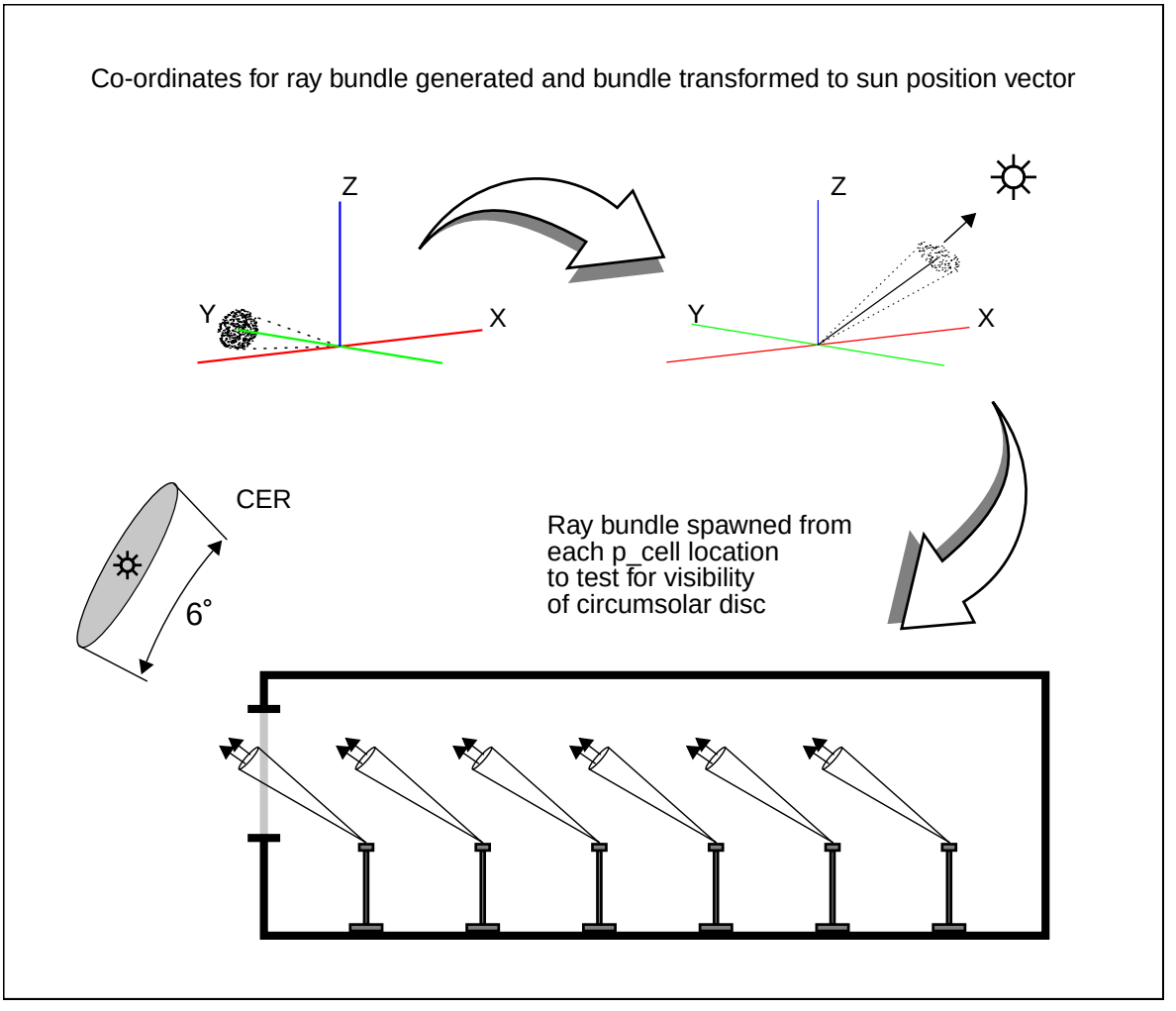

Figure 4-29. Generating ray bundles to test for visibility of circumsolar disc

Here, each of the distributions, with the exception of p_cell 3, appears fairly symmetric about the 0% line, and, as with the un-filtered data, the main body of the distribution is contained within the range ±17.5%. For all p_cells, with the exception of number 3, the MBE is very low, and the RMSEs are never greater than 17%. This is a significant improvement over the un-filtered data (Figure 4-10).

The predictions from the 'potentially unreliable' (CS6+VIS) photocell-scan combinations are very different, Figure 4-31(b). Note that not only are the MBEs much larger than for the 'reliable' data, but they are all positive. This is because over prediction can give (positive) RERs » 100%, but the RER

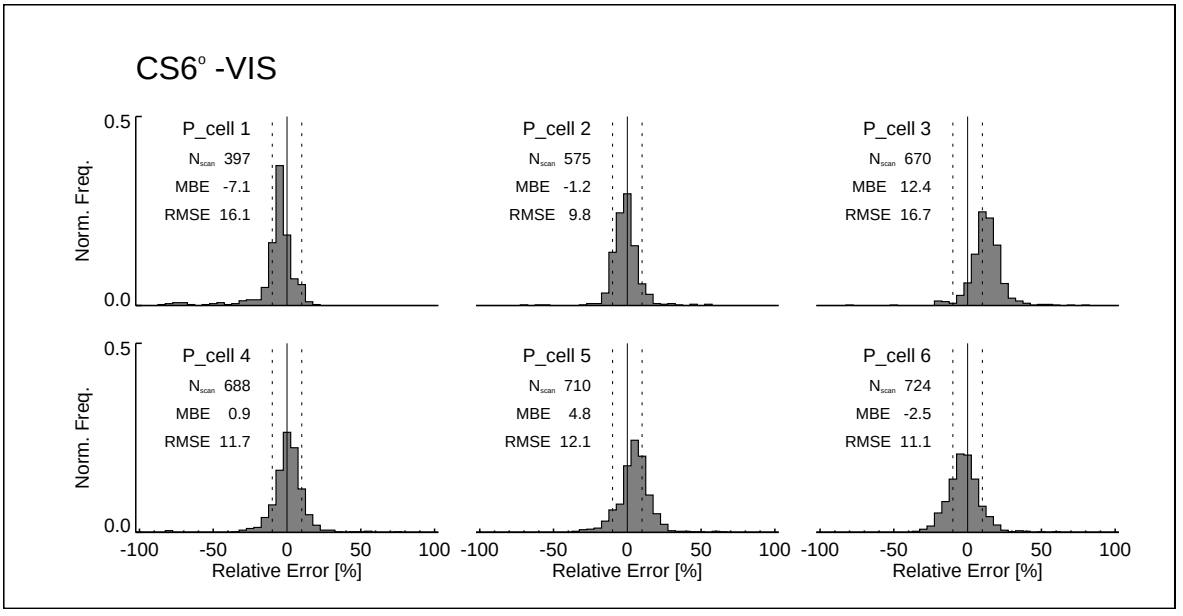

Figure 4-30. RER histograms for 'reliable' data

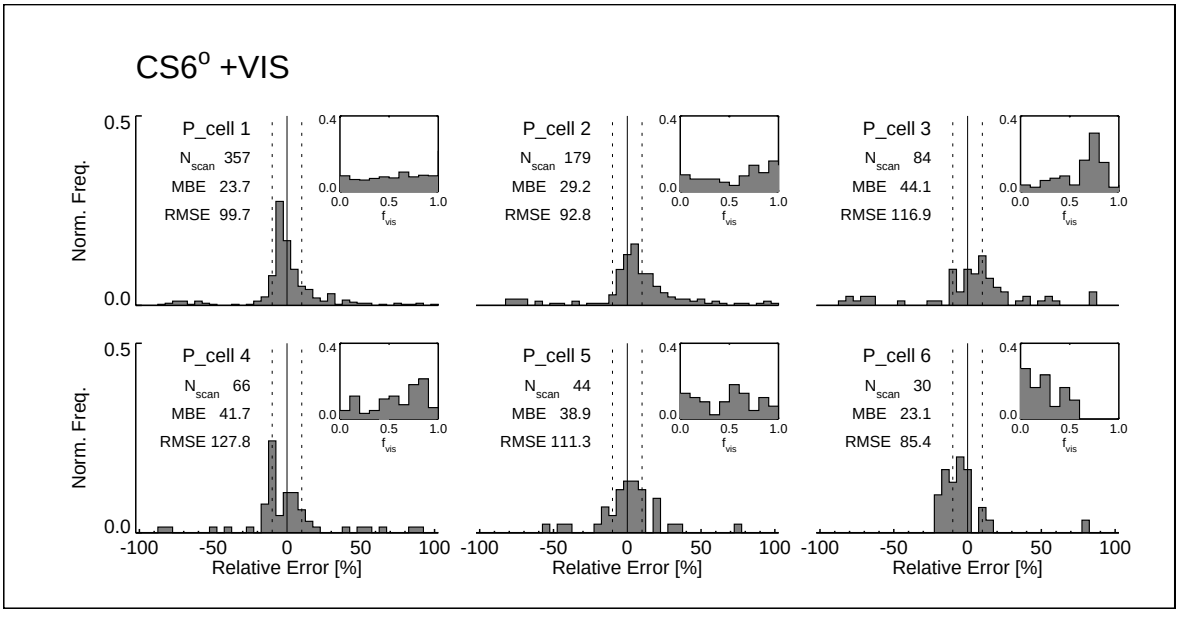

Figure 4-31. RER histograms for 'potentially unreliable' data

limit for under prediction is -100%. Significant over prediction in illuminance can occur when a photocell was predicted to be in sun when in reality it was in shade. The smallest of differences in geometry between the model and the actual office could cause this. The small inset histogram for each photocell shows the distribution in the fraction of the 6˚ CER disc that was visible for each photocell. For example, at the back of the room (p_cell 6) the photocell never 'saw' more than about half of the CER disc.

The overall effectiveness of the partition can be better appreciated from the plots in Figure 4-32. For the upper plot (a), the absolute relative error - for all the photocells together - was aggregated into bins of size 10%. The 'reliable' (CS6˚-VIS ■) and 'potentially unreliable' (CS6˚+VIS ■) sets are plotted alongside, and their sum[12] is given by the box that bounds each pair. The last bin (100 - Inf.) is for all absolute RERs greater than 100%. The lower plot (b) gives the number of 'reliable' and 'potentially unreliable' samples as a fraction of the total number. For example, there were nearly 3,000 cases where the absolute relative error was in the range 0 - 10%, of which nearly 400 (i.e. ~0.15 of the total) were classed as 'potentially unreliable' because the CER was visible from the photocell. For |RERs| > 40%, the greater part of the total number are classed as 'potentially unreliable', and for |RERs| > 90%, all of the cases are classed as 'potentially unreliable'. It is clear from the Figure 4-32 however that many accurate illuminance predictions are also classed as 'potentially unreliable'.

One might speculate that it is possible to include the most heavily overcast skies - where large luminance gradients about the solar position are unlikely - as 'reliable' even though the (dull) circumsolar region was visible to the photocell. To test this premise, the partitioned sets were stratified by sky clearness index bin and the MBE and RMSE for each new set evaluated, Figure 4-33. For both MBE and RMSE, the accuracy for the 'reliable' set is

12. The sum is identical to Figure 4-12 given in Section 4.2.2.

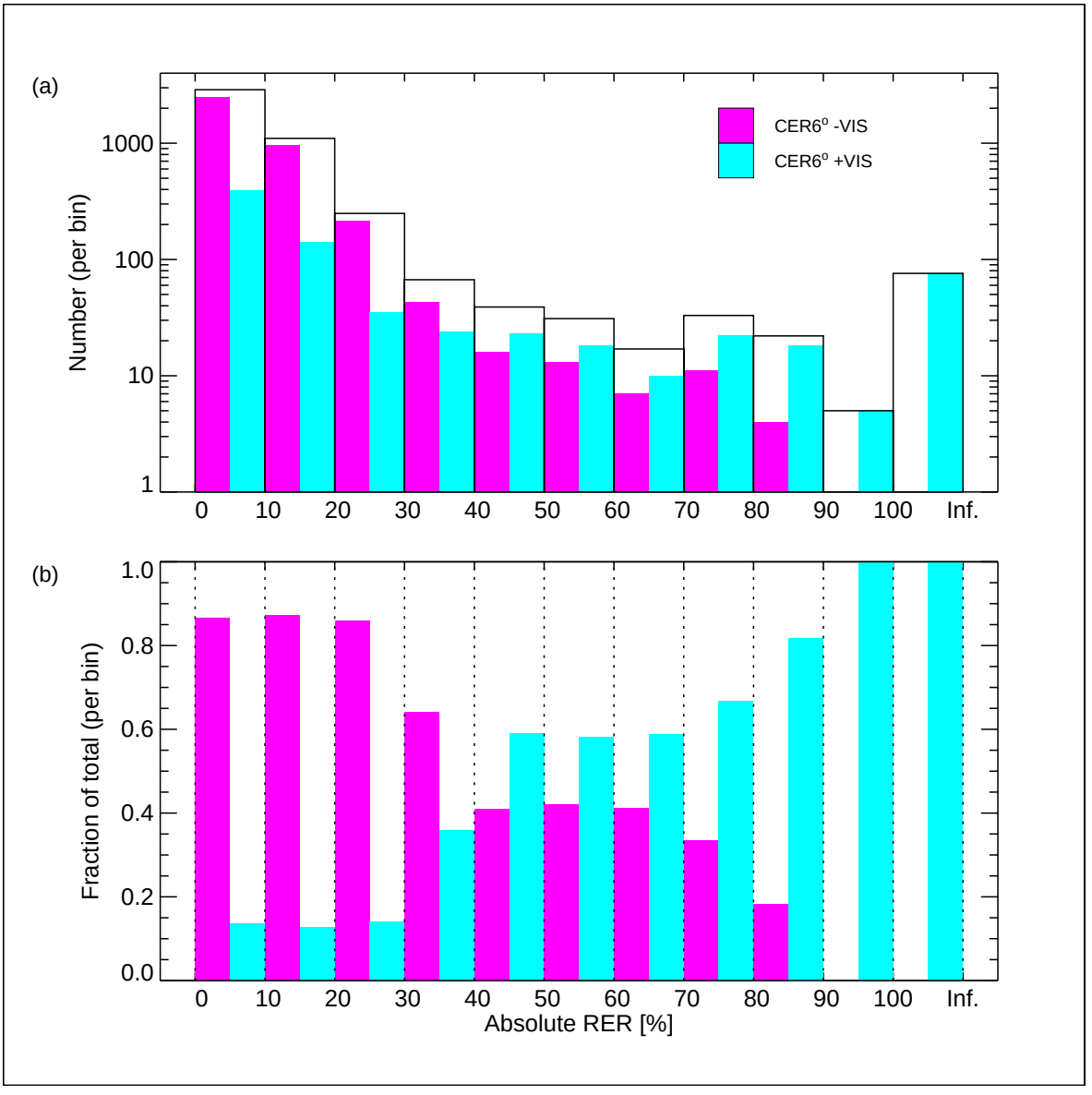

Figure 4-32. Partitioned dataset

always better than for the 'potentially unreliable'. As might be expected, the difference is less for the overcast skies (bin 1), but it is nevertheless significant. So the premise is considered to be false.

In the last of the plots for this section, the RER at each photocell is plotted together with the time-series of global horizontal, diffuse horizontal and vertical South illuminances. A pair of plots are given for each of the 27 days. They are grouped together in Figure 4-34 to Figure 4-37. Here, the relative

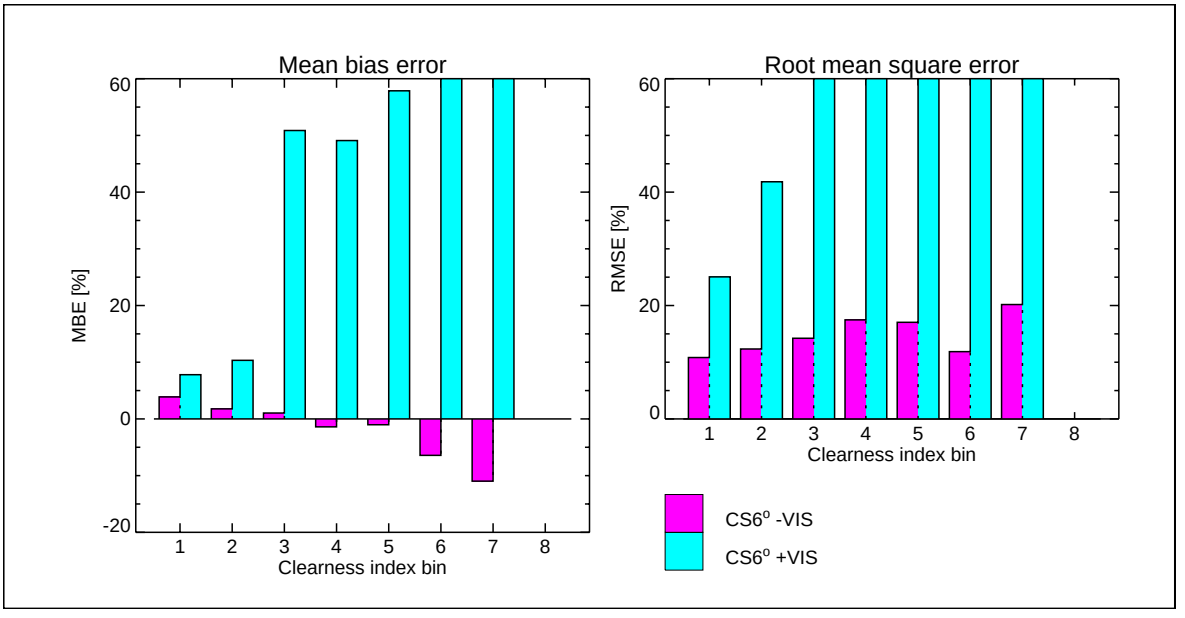

Figure 4-33. MBE and RMSE stratified by clearness index

error at each photocell is marked at the time of the measurement by a shaded square. The 'reliable' photocell-scan combinations are shaded magenta (■) and the 'potentially unreliable' combinations are shaded cyan (■). RERs less than -50% or greater than 50% are plotted at -50% and 50% respectively. The illuminance predictions were made every 15 minutes, which was the sampling frequency of the sky scanner. The three external illuminances values however are plotted at 5 minute intervals, which was the interval at which these quantities were obtained. Note that for heavily overcast skies, the lines for the global horizontal and diffuse horizontal illuminances are superposed.

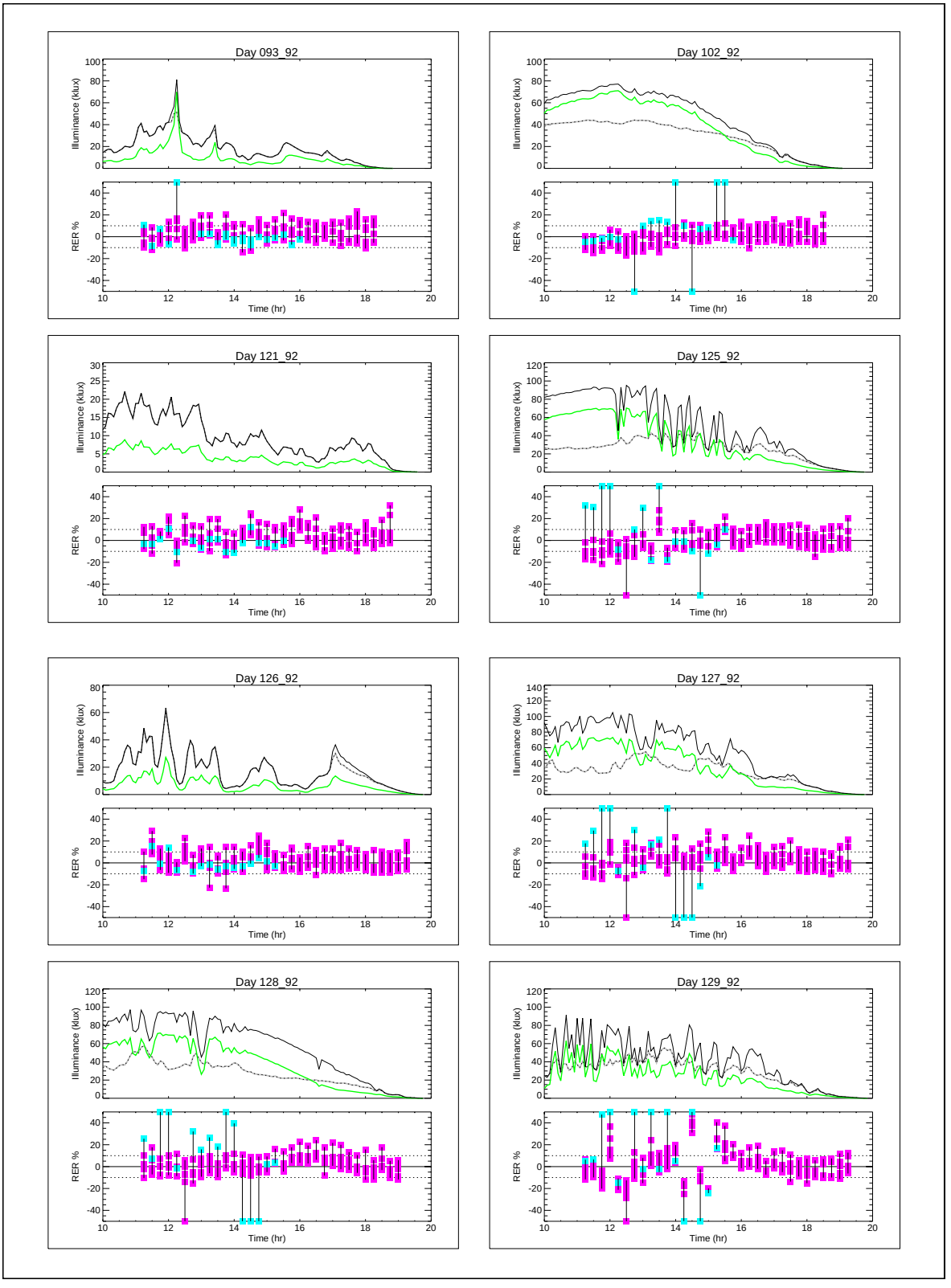

Figure 4-34. Illuminance RER time-series

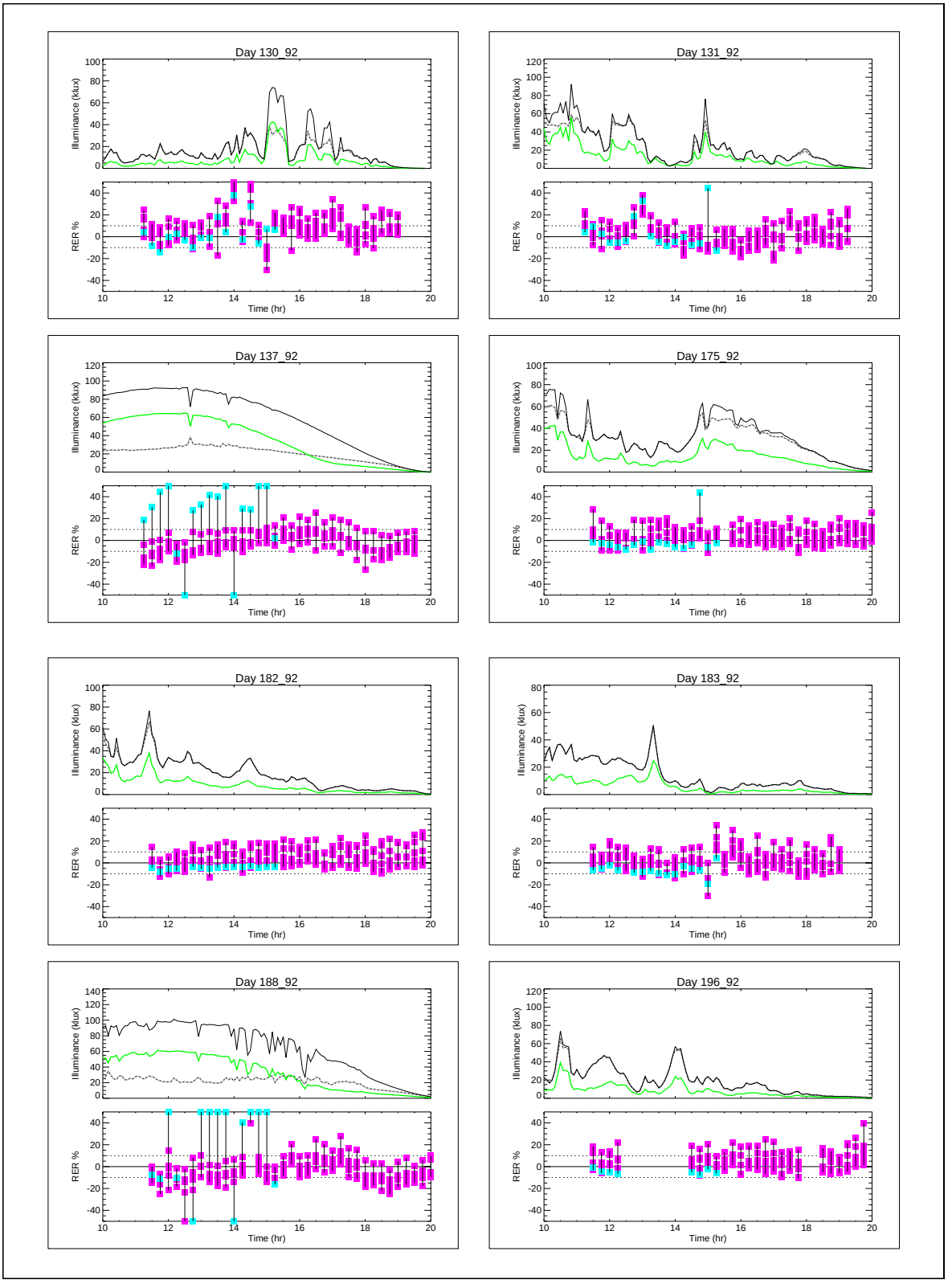

Figure 4-35. Illuminance RER time-series

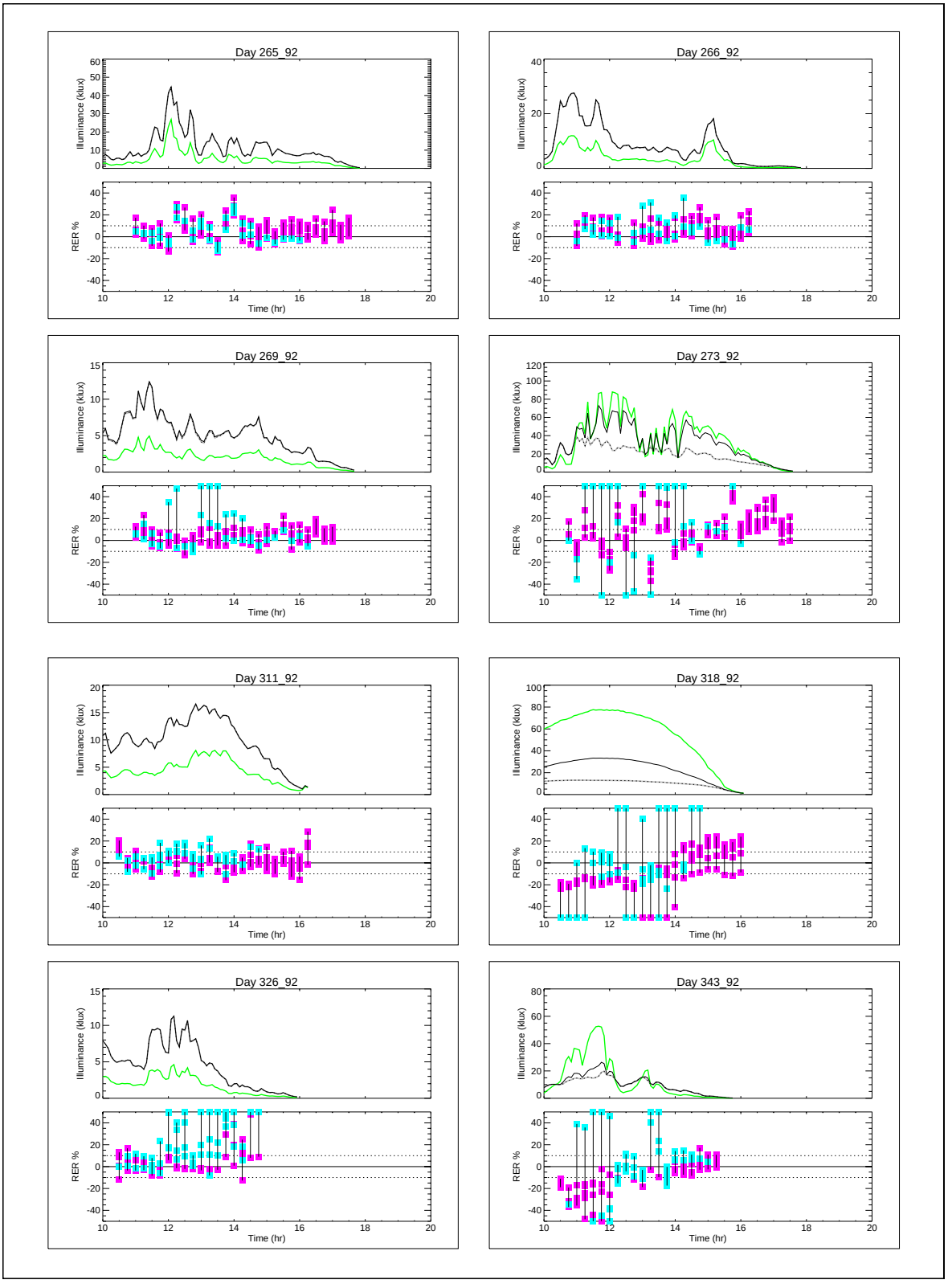

Figure 4-36. Illuminance RER time-series

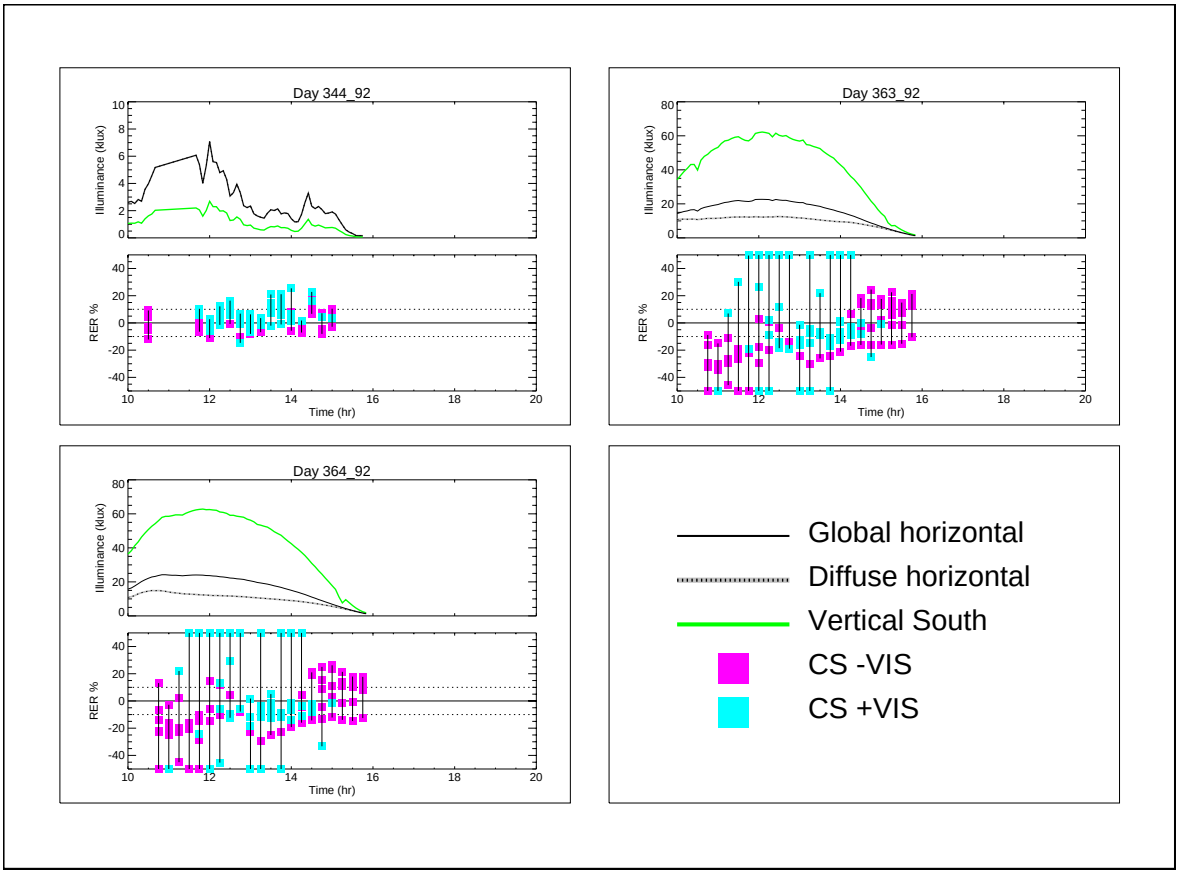

Figure 4-37. Illuminance RER time-series

From the plots in these figures, the following features are observed:

- The RERs were generally much lower for overcast skies than for non-overcast skies.
- The majority of instances when an RER was outside of the range ±25% occurred for non-overcast skies.
- When these occurred, most were identified as ‘potentially unreliable’.
- There is evidence to suggest that the occasional poor accuracy from ‘reliable’ data might be related to rapidly varying sky conditions. This is suggested by occasional large variation in the 5 min. external quantities time-series, e.g. for periods on days 129_92 and 273_92.

- Something of the sinusoidal character discerned in the plots for external quantities on clear-sky days (Figure 4-2 - Figure 4-5) is apparent in the pattern of the internal RERs for the same period.

The findings for this section are summarised below.

4.5.3 Summary

The partition of the validation data into 'reliable' and 'potentially unreliable' sets, based on visibility of the (6˚) CER, has been demonstrated and considerable evidence has been presented to support the hypothesis given in Section 3.2.7. Based on that evidence, it is proposed that intrinsic accuracy of the *Radiance* illuminance calculation is indicated by the characteristics of the 'reliable' set, and that the characteristics of the 'potentially unreliable' set are largely dominated by one or more of the source visibility related errors listed in Table 3-9. There were however, some cases where 'reliable' data resulted in poor accuracy predictions. In the following sections, attempts to further reduce or eliminate these instances are described and evaluated.

The positive bias in the illuminance predictions at p_cell 3 was not greatly improved by partition of the validation dataset, even though the scatter was much reduced. This suggests that this photocell suffered from a calibration error, or similar fault, during all, or most, of the measurement period for this dataset. The experimenters have acknowledged that this is a possibility.[13]

4.6 The ambient parameter resolution revisited

Thus far, the analysis of the error characteristics for the illuminance predictions has concentrated on identifying potentially unreliable photocell-sky combinations, and then eliminating them from the overall assessment of the accuracy of the calculation. But what of the *Radiance* illuminance calculation itself - might it be possible to obtain higher accuracy predictions

13. Private communication - M. Aizlewood, BRE.

by increasing the resolution of one or more of the simulation parameters? Also, is there the potential to achieve comparable accuracy to the basecase simulations using lower resolution parameters in a computationally less demanding (that is, faster) calculation?

Given the high dimensionality of the parameter space for the ambient calculation, it was not practicable to repeat for the entire validation sample the process that was used to select the basecase parameter set (Section 3.3). Instead, the illuminance predictions for the entire validation sample were repeated using two new sets of ambient parameter combinations. One set, called lo-amb, of much lower resolution than the basecase set. The other, called hi-amb, of much higher resolution than the basecase set. The new parameter combinations that were used - including the basecase set for comparison - are given in Table 4-4. The change from the basecase to the

Parameter	Hi-amb	Lo-amb	Basecase
ad	4096	1024	2048
ab	7	7	7
ar	4	1	2
as	64	16	32
aa	0.05	0.2	0.10

Table 4-4. Ambient parameter settings (av=0)

hi-amb set was effectively a doubling of the resolution of each parameter. Similarly, the change from the basecase to the lo-amb values was a halving of the resolution. The ambient bounces parameter (**ab**) was fixed because without a sufficient number of levels of inter-reflection, the calculation could never converge to an accurate value - regardless of the resolution of the other ambient parameters.

4.6.1 Low ambient parameter resolution

The results from the lo-amb simulations are given as histogram plots of the (binned) predicted relative error, Figure 4-38. As with the predictions that were obtained using the basecase set (Figure 4-30), all photocell-sky

combinations where the 6˚ circumsolar disc was visible have been eliminated from the sample.

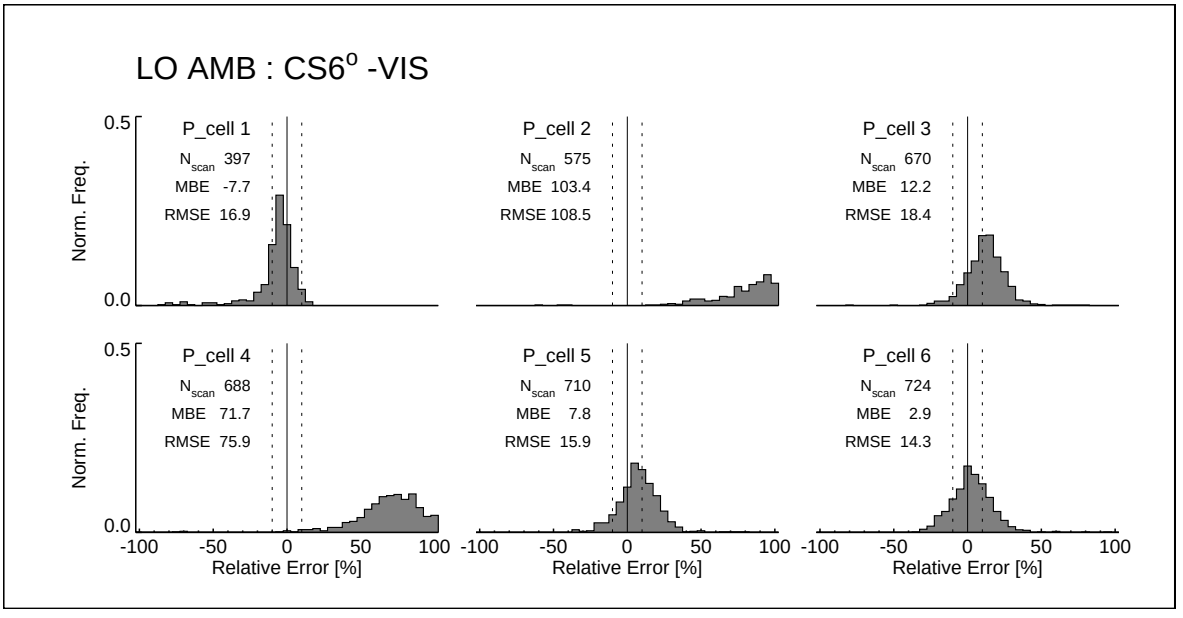

Figure 4-38. Lo-amb results

Most readily apparent in Figure 4-38 is the very poor accuracy for the illuminance predictions at photocells 2 and 4. For the other photocells however, the overall predictions were only slightly worse than those obtained using the basecase parameter set. The pattern in the relative error distribution across the photocells indicates that, for this parameter combination, the irradiance interpolation algorithm has performed very poorly. Errors of this type were described in Section 2.5 on page 24. When these errors occur, the predictions can be very sensitive to the order of the calculation points that are passed to the **rtrace** program. To demonstrate this, the low-amb simulations were repeated, but now the photocell points were passed in *reverse* order, Figure 4-39. The illuminance predictions for this scenario are shown in Figure 4-40. The accuracy shown here is significantly poorer than that for the same parameter combination with the points in the default order (Figure 4-38). This is because the entire inter-reflection calculation depends - to a greater or lesser degree - on the first

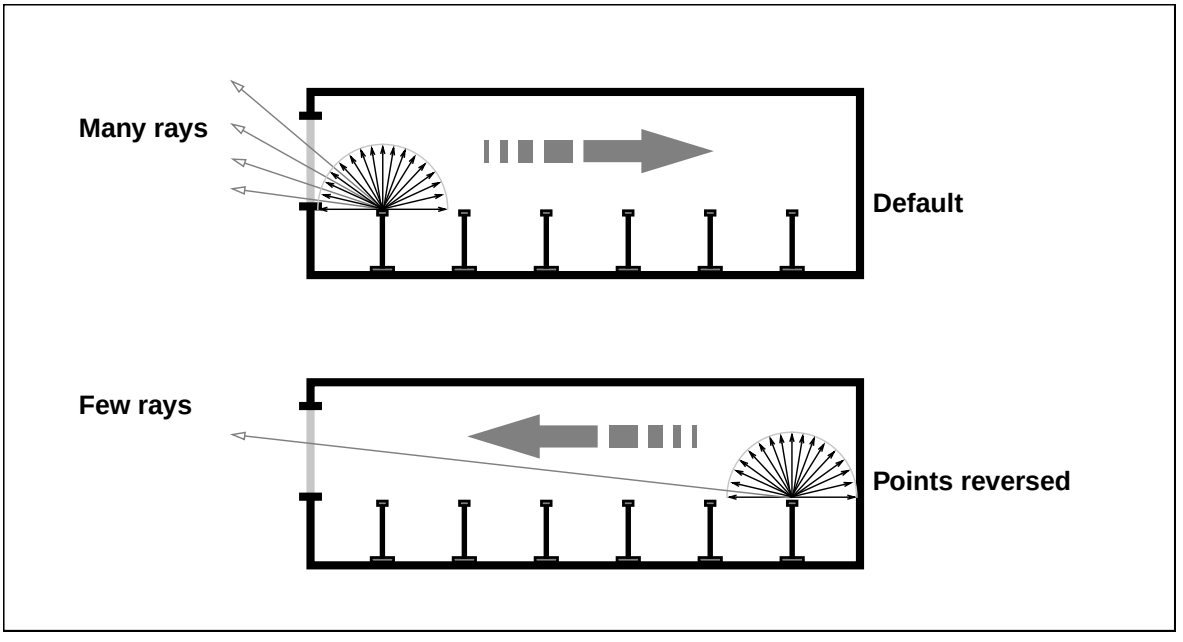

Figure 4-39. Photocell points reversed

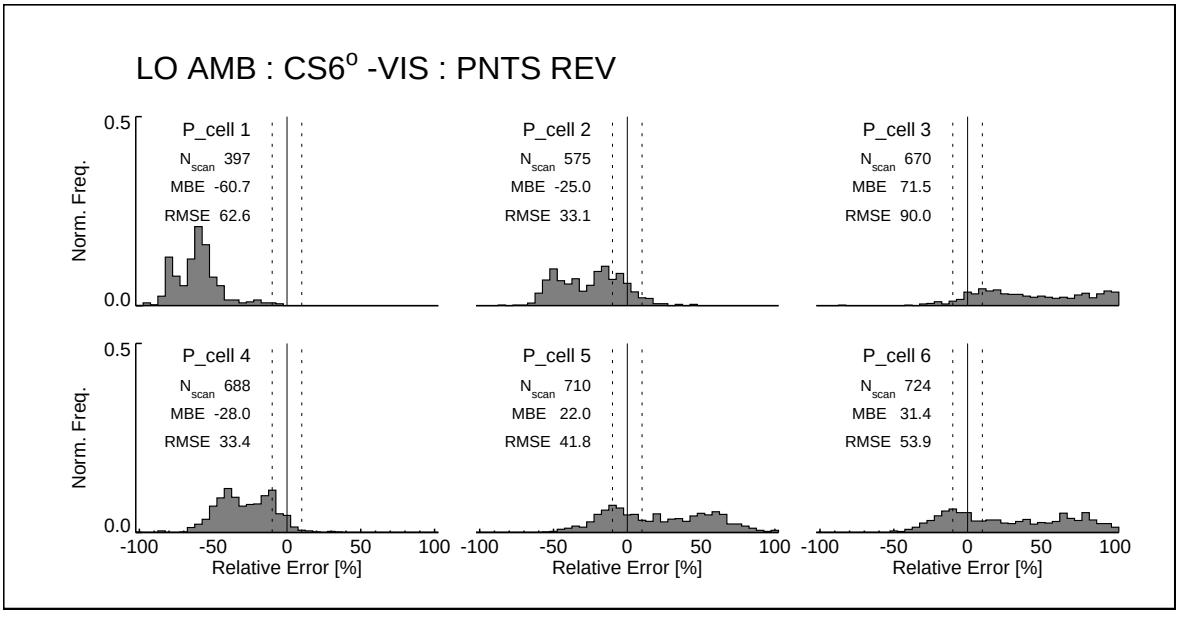

Figure 4-40. Lo-amb results with calculation points reversed

estimates of the indirect irradiance gradient. The gradient is first estimated from the sampling rays that are spawned from the *first* point of calculation,

which here, was the first photocell location in the list of positions supplied to **rtrace** in the simulation shell script. For the default order, it was p_cell 1 nearest the window. When the points were reversed, it was p_cell 6 at the back of the room. The same number of initial sampling rays were used for both sets of (low resolution parameter) simulations. It is clear however, that the number of the spawned rays that sampled the window area was much greater from p_cell 1 than from p_cell 6. In fact, since the indirect hemispherical sampling has a cosine weighting in the distribution, the probability that a ray samples the glazing can be determined from hemispherical projection renderings[14] of the office from the photocell locations (see Figure 4-17 on page 119). In the rendering of the hemispherical 'view' from p_cell 1, the glazing occupies ~16% of the total (circular) field of view. The glazing therefore is sampled by ~16% of the rays spawned from p_cell 1. From p_cell 6 however, the 'view' of the glazing is much smaller: only about 0.3% of the total (circular) field of view. The probability that the glazing will be sampled by rays spawned from each of the photocell locations is given in Table 4-5.

Photocell	1	2	3	4	5	6
Probability that glazing is sampled	1	1/2.5	1/6	1/13	1/26	1/50

Table 4-5. Glazing sampling probability at photocell locations normalised to 1 at p_cell 1

4.6.2 High ambient parameter resolution

The high resolution ambient parameter combination resulted in barely significant improvement over the basecase set, Figure 4-41. Only at p_cell 1 was the improvement marked to any degree: from MBE = 7.1% (basecase) to -2.4% (hi-amb). For p_cells 2 to 5, the change in either MBE or RMSE was never greater than 1.2%. At p_cell 6, the MBE shifted from -2.5% (basecase) to 3% (hi-amb) - a change of 5.5%, but hardly important. That this should

14. This projection has the same cosine weighting that was used for the sampling distribution. Therefore, equal areas in the rendering are sampled by, on average, equal numbers of rays.

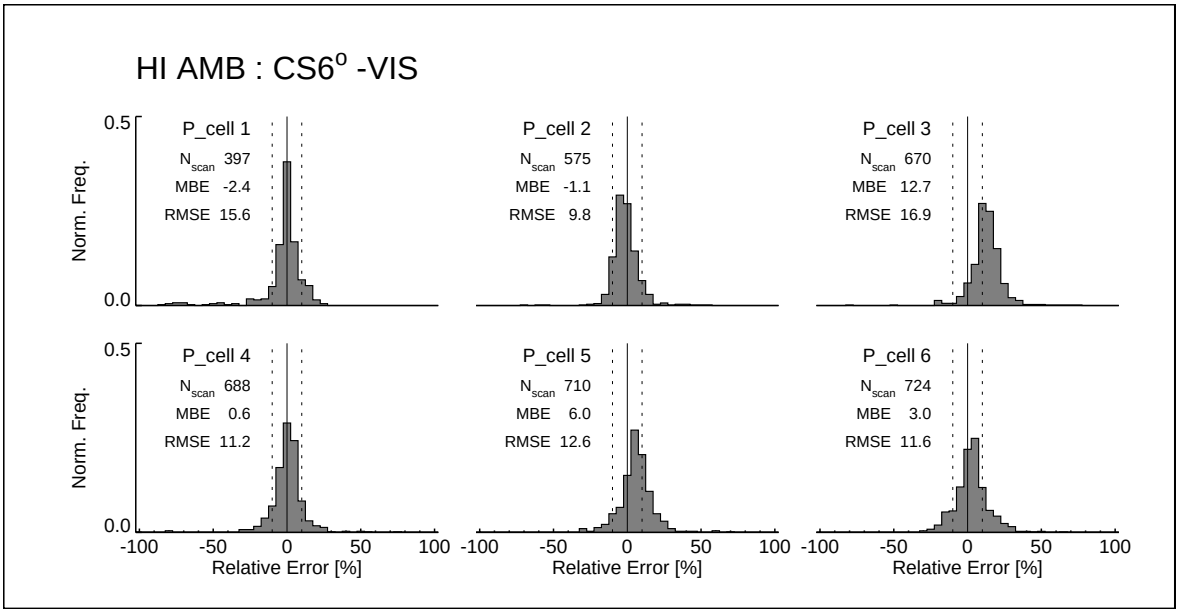

Figure 4-41. Hi-amb results

be the case, even though the high resolution calculation spawned ~10x more sampling rays than the basecase calculation, suggests that each of the simulations had, for practical purposes, converged to a final value with the basecase parameter set.

4.6.3 Summary

The results for this section are summarised schematically in Figure 4-42. The abscissa line represents an idealised continuous variation in the resolution of the ambient parameter combination - actually a variation in 4 dimensional parameter space (**ab** was constant). From the three point plot, the trajectory of the line from point B to point H can be fairly certainly estimated: an increase in the resolution of any of the four parameters would have resulted in a prediction that offered no significant improvement over the basecase, whilst taking longer to compute.

Would it be worthwhile to investigate the (4D) parameter space that lies between the points L and B? Given the scope of the problem - many possible combinations of 4 parameters - and that the absolute best that could be

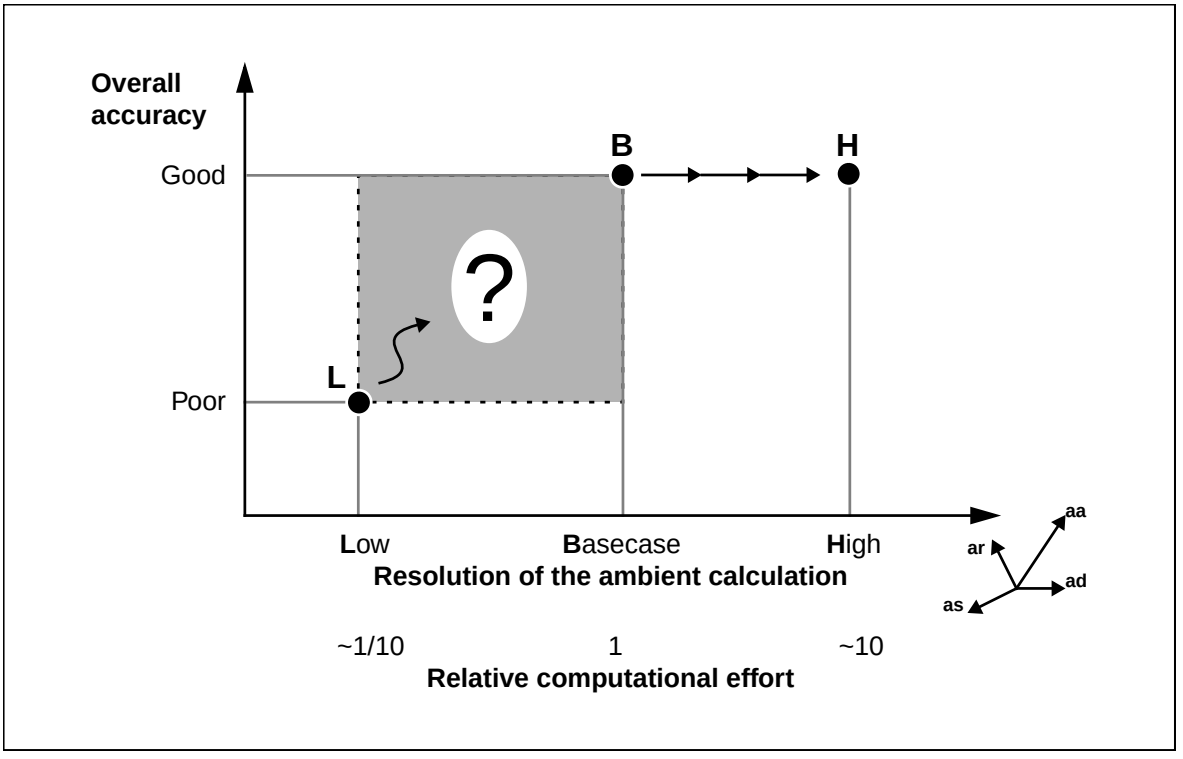

Figure 4-42. Accuracy versus parameter resolution

achieved would be less than a factor 10 increase in computational speed, the answer offered is no. The advances in the speed of computers shows no sign of abating, and the present generation of processors are 10x or more faster than the machine that was used for the bulk of the validation work described here. What of the need though to evaluate an annual profile for internal illuminance, say at an hourly time-step? For this, the internal illuminance due to 4000 or so unique skies and sun configurations would need to be computed. Presented with this magnitude of individual illuminance predictions, it could be argued that the potential for quicker simulations should be investigated. It may not however be necessary to perform the computationally demanding part of the calculation more than a few hundred times - regardless of the number of unique sky/sun configurations that, thereafter, need to be evaluated. A technique that achieves this is described in Chapter 6.

4.7 The circumsolar exclusion region revisited

The application of the rejection criterion for potentially unreliable photocell-sky combinations - visibility of a 6˚ circumsolar disc - elicited a marked improvement in the assessment of the overall accuracy of the illuminance predictions (Section 4.5). The original hypothesis appears therefore to be vindicated on the basis of this improvement and the supporting evidence. A CER diameter of 6˚ was chosen because this was the acceptance angle of the instrument that measured the direct normal illuminance. A CER of smaller diameter might reasonably be expected to be less successful at identifying unreliable photocell-sky combinations in the validation data. But would a larger diameter CER pick-out additional unreliable photocell-sky combinations? Also, is there evidence to indicate that uncertainty in the circumsolar sky luminance may exist over regions greater than 6˚ for some skies? The following section describes a rendering-based analysis that compares the measured and modelled sky luminance distributions for an overcast and a clear sky. Differences between measured and modelled sky luminances are quantified.

4.7.1 Luminance gradients in the circumsolar region

Comparison between the scanner-measured sky luminance and the resulting continuous sky luminance distribution is not straightforward. One quantity that can be obtained is the difference between the measured sky luminance and the luminance of those patches of the continuous sky that are coincident with the scanner measurement pattern. For this, a series of renderings for a 40˚ by 40˚ region centred on the sun position were generated for one overcast day (121_92) and one clear sky day (318_92). Each rendering was false-coloured to show the sky luminance; below horizon ‘sky’ is shaded gray.

First, the clear sky day, Figure 4-43. The upper sequence shows the continuous sky luminance distribution that was used in the *Radiance* simulations for times 12h00 to 14h45 for day 318_92. The lower sequence

shows the measured sky luminance (circular patches) overlaid onto the continuous model sky. Recall that to transform from the scanner measurements to the *Radiance* continuous sky brightness distribution, two interpolation mechanisms were applied. Firstly, the scanner measurements were interpolated to a regular array compatible with the brightdata format (Section 3.2.5 on page 67). Then, *Radiance* used its own bi-linear interpolation to estimate in-between (i.e. continuous) values from the brightdata array. Note that for most of the instances in the sequence, the (continuous) circumsolar sky luminance has a diamond-like shape. This pattern is a characteristic artifact of a bi-linear interpolation about a peak value.

It is apparent from the sequence showing the scanner measurements that there is often significant difference between the luminance of the continuous model sky and the measured patches. This is to be expected because the scanner measured an average sky luminance across an 11˚ field. Indeed, it would be highly un-realistic to model the measured sky as 11˚ patches of constant luminance (where measured) with some, say, interpolated value for the regions not covered by the scanner. What the difference between the measured and modelled sky luminance distributions does give however is *some* indication of the degree of uncertainty in the distribution. The continuously modelled sky reproduces the likely form of a clear-sky circumsolar region, at least approximately. But the actual sky luminance values within each measurement patch - and in between - cannot be said to describe the conditions as they occurred at the time. Compare this with the rendering sequence for an overcast sky, Figure 4-44. For these sky conditions, it was likely that there was little significant difference between the measured and modelled sky luminance distributions.

A simple numerical comparison between the measured and modelled 40˚ by 40˚ circumsolar regions was achieved by using the non-zero luminance values in the scanner image to identify the coincident pixels in the

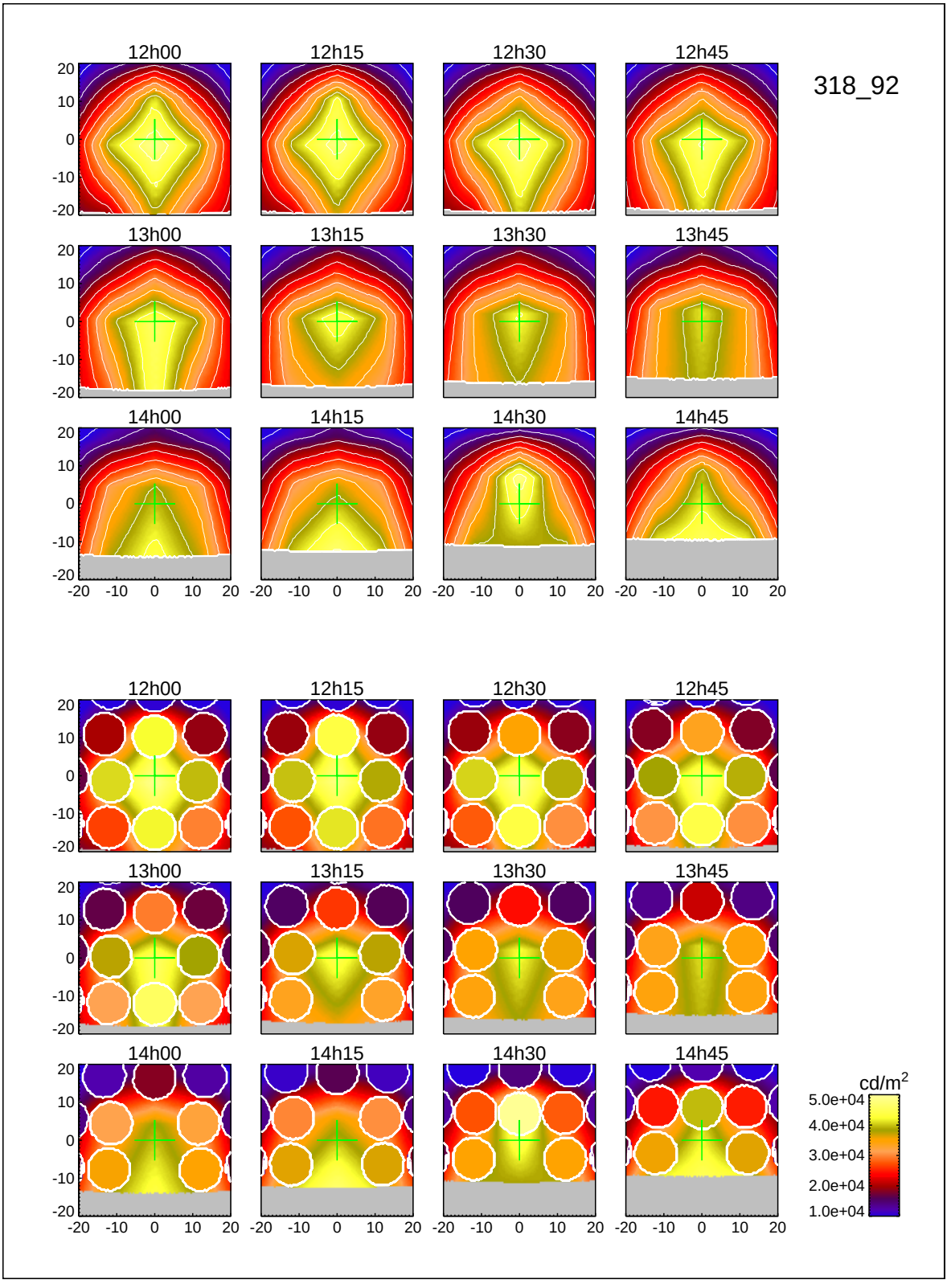

Figure 4-43. Renderings of model and measured skies for day 318_92

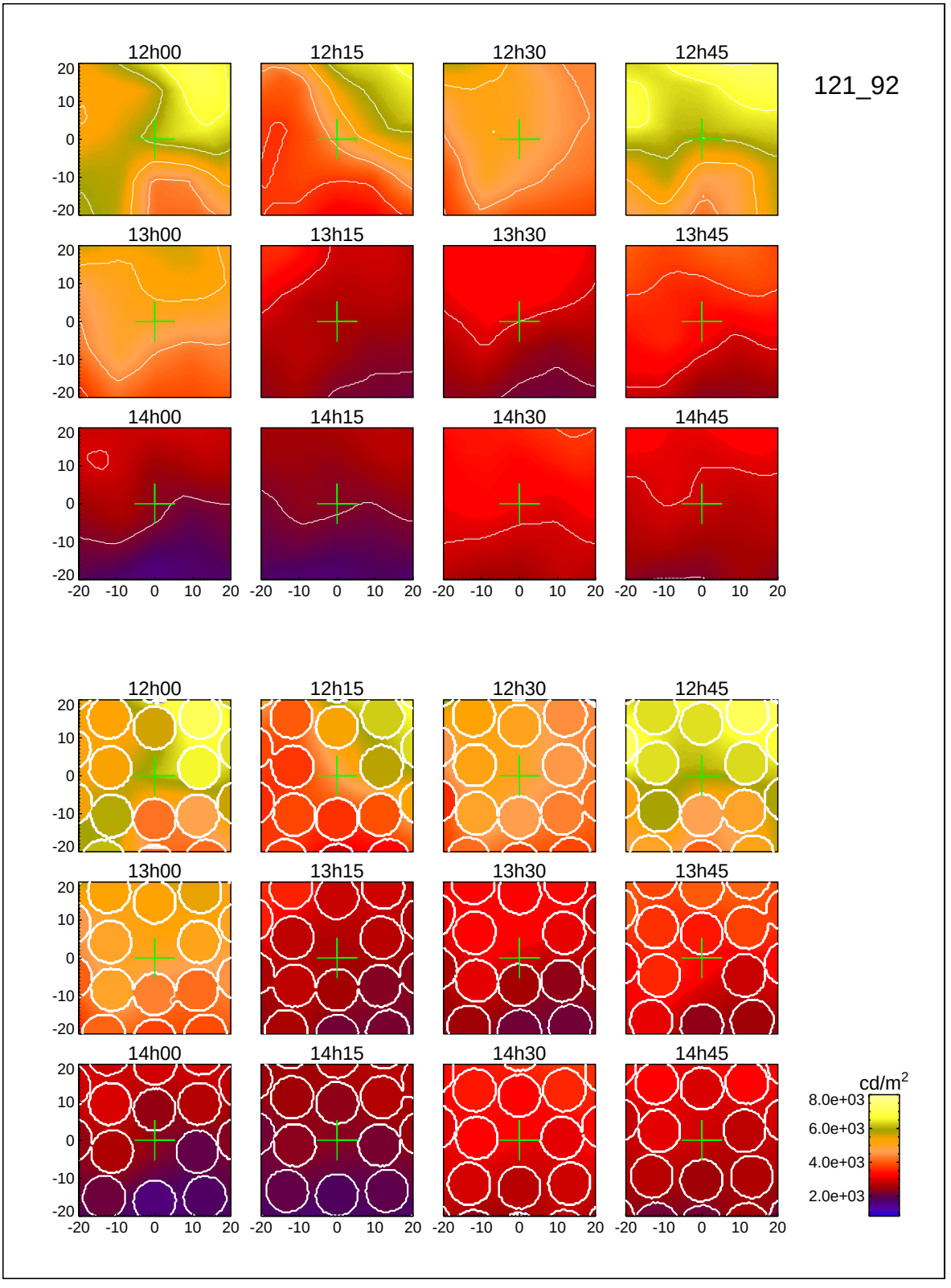

Figure 4-44. Renderings of model and measured skies for day 121_92

continuous sky renderings. In this way, the mean bias difference (MBD) and the root mean square difference (RMSD) between the coincident scanner-pixels and the continuous-pixels for each of the 40˚ by 40˚ renderings was obtained, Table 4-6. The RMSD should be taken as giving some indication of the uncertainty in the luminance distribution in the 40˚ by 40˚ extended circumsolar region. The MBD for the clear sky day was always positive and ranged from 3% to 10%. This is consistent with normalization of the model sky when the circumsolar sky luminance is under-estimated (Section 3.2.6). The RMSD between coincident pixels for the clear sky day was quite large: 49% to 103%. Both the MBD and RMSD were very much lower for the overcast sky day. This limited examination suggests that uncertainty in the circumsolar sky luminance distribution may, for clear skies, extend over regions larger than the 6˚ CER. In the next section, the sensitivity of the overall errors for internal illuminance prediction to the CER angle is examined.

Time	Clear sky 318_92		Overcast sky 121_92	
	MBD%	RMSD%	MBD%	RMSD%
12h00	6.8	51.3	2.0	22.3
12h15	6.9	48.6	1.6	11.5
12h30	4.9	45.0	0.2	8.6
12h45	5.0	62.2	0.7	5.4
13h00	4.4	73.3	0.2	4.0
13h15	4.2	78.9	-0.1	3.8
13h30	3.0	53.0	0.5	4.5
13h45	3.1	60.3	0.3	4.5
14h00	5.5	60.0	0.2	5.6
14h15	7.0	51.7	-0.3	4.3
14h30	9.7	103.0	0.1	6.0
14h45	10.0	96.0	0.4	3.4

Table 4-6. Difference between measured (patch) luminances and equivalent patches from continuous sky luminances

4.7.2 Errors as a function of CER angle

A modified form of the visibility test described in Section 4.5.1 was repeated for a number of CER angles covering the range 0.2˚ to 16˚. The diameters 0.2˚ to 2˚ were in 0.2˚ steps, and the 2˚ to 16˚ range was covered in 2˚ steps. In preference to presenting another 16 histograms plots[15] (one for each additional CER angle), a more concise presentation was devised. The results for each photocell are shown in Figure 4-45. Plotted on the graphs, in a vertical line at each CER angle tested, are the RERs where the CER was not visible from the photocell. From each of the RER distributions, the following quantities were derived and plotted to show their variation with CER angle:

- the mean bias error;
- the room mean square error;
- the maximum and minimum RERs; and,
- the 2nd and 98th percentile values for the RERs.

Immediately apparent in these plots is the improvement in the overall accuracy over the complete sample results (CER = 0˚) at the first non-zero CER angle (0.2˚). This is to expected since the main effect here is the removal of large positive RERs which would occur when a photocell in shade was predicted to receive direct sunlight - as might happen if there was misalignment between model and reality. This effect is of course independent of the disc diameter. Surprising perhaps, is the relative insensitivity of the overall MBE and scatter (i.e. standard deviation) to the CER angle, for photocells 3 to 6. Recall that for the complete sample, the MBE was always skewed to the positive because of the occurrences of RER » 100%. With these eliminated (CER > 0˚), any subsequent improvements with progressively increasing disc diameters do not figure too greatly in the MBE because they affect a relatively small number of cases: the majority of the predictions were, in any case, good.

15. That is, of the type shown in Figure 4-30.

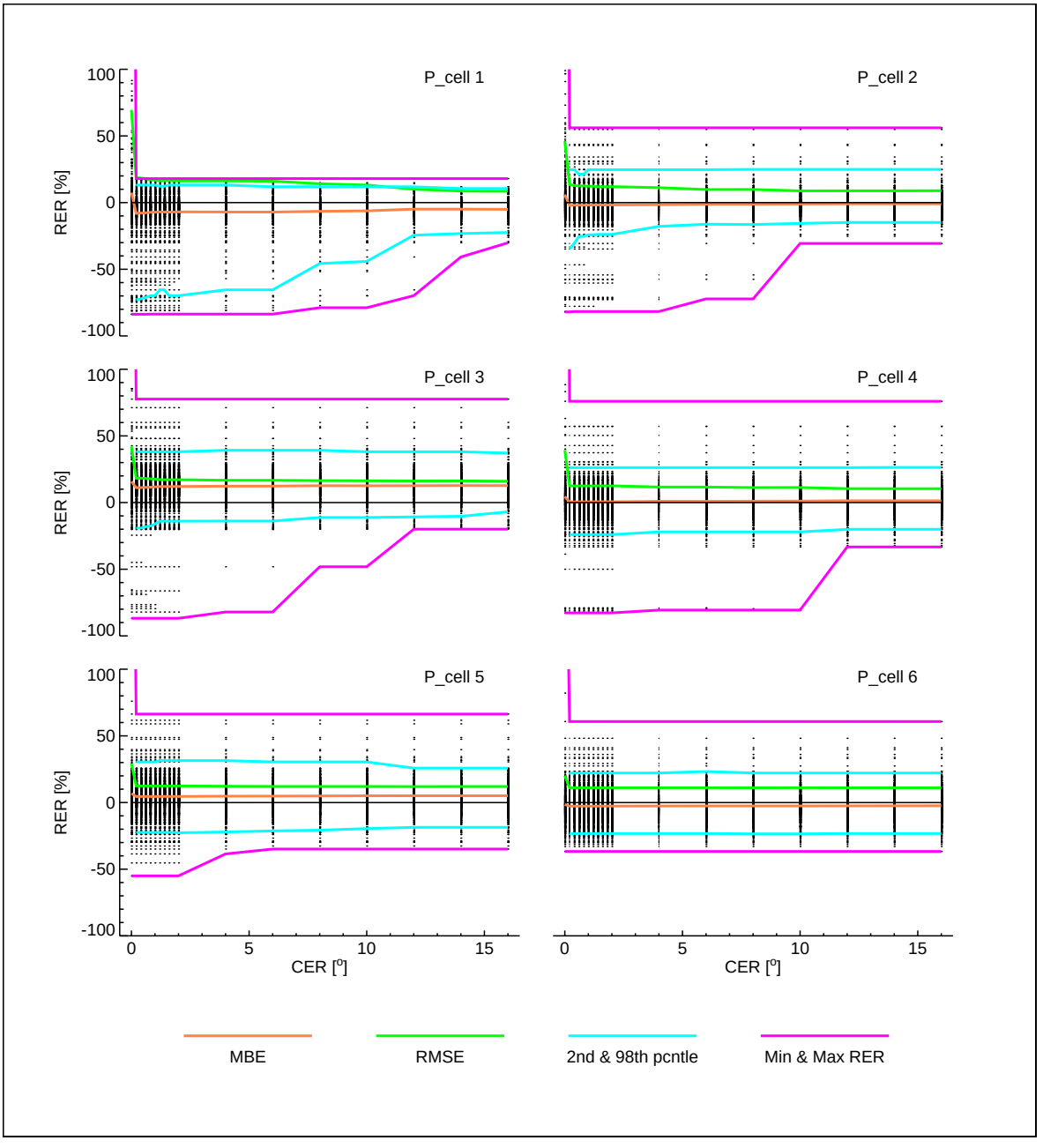

Figure 4-45. Sensitivity of errors to CER angle

A conspicuous feature of the plots, for all 6 photocells, is the variation of the maximum positive and negative RERs. After removal of the highest positive RERs (CER = 0.2˚), the maximum positive RER thereafter remains constant for all CER angles. This insensitivity means that the maximum positive RERs were not related to uncertainties in the either the luminance gradient

across the circumsolar discs or their absolute brightness. In contrast, the maximum negative RER shows gradual improvement with increasing disc diameter - this is so for all photocells (except p_cell 6), though not to the same degree. This is consistent with under-prediction of the circumsolar sky luminance (Section 3.2.6).

Finally, these results are further reduced to an overall summary plot that shows, for the entire sample, the fraction of the sample that is within the RER limits of ±10%, ±15% and ±20% for all the CER angles tested, Figure 4-46. Also shown, is the fraction of the total sample remaining at each CER angle. For example, for the entire sample (CER = 0˚), approximately 0.64 (that is 64%) of the total number of predictions are within ±10% of the measured value. And about 0.88 (that is 88%) of the predictions are within ±20% of the measured value. In view of the fact that p_cell 3 may have suffered from a calibration error (Section 4.5.3), the results for the total sample minus the measurements at p_cell 3 are shown also. Eliminating these measurements elicits a marked improvement for all three RER ranges, and at all CER angles. The change from CER = 0˚ to CER = 0.2˚ elicited the greatest 'step' improvement. Successive increases in the CER angle resulted in only marginal increase in the fractions of the total within the RER ranges, at the expense of reducing the sample size.

4.7.3 Summary

This study has shown the results are less sensitive to the size of the CER than may have been expected. Indeed, what emerges as most significant is the elimination of all cases where the photocell could 'see' the sun, i.e. for all CER > 0˚. Sensitivity to CER angle was greatest for p_cell 1 which, of course, had the greatest 'view' of the sky. The insensitivity of the 2nd and 98th percentile lines to changes in CER angle indicates that, although outliers may be affected, the overall RER distribution was largely unchanged. Only for p_cell 1 did the 2nd percentile line show any significant variation with CER angle.

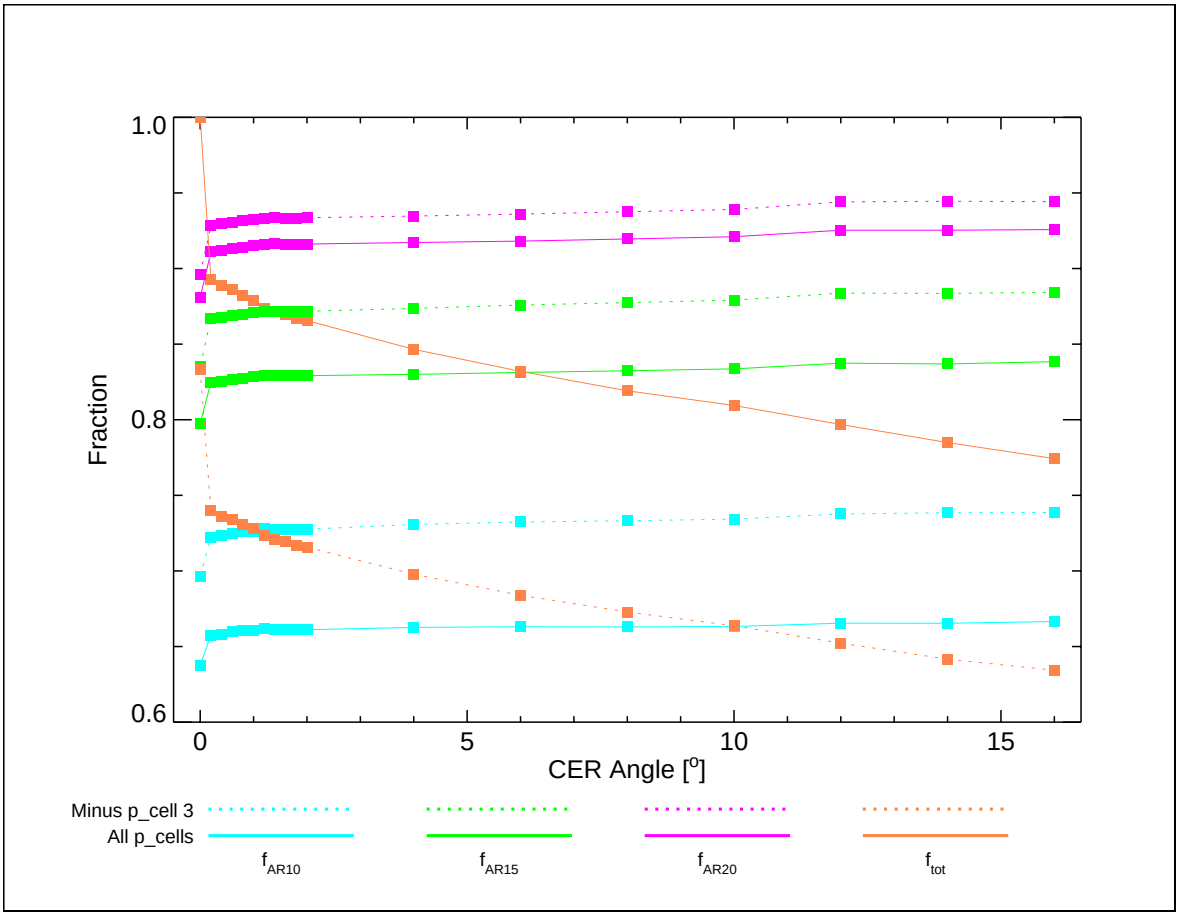

Figure 4-46. Fractions versus CDOA

4.8 Conclusion

This validation study had demonstrated that the *Radiance* system has the potential to accurately predict daylight illumination levels under naturally occurring conditions for a wide range of sky types. The relative error for the majority of the predictions was commensurate with the precision of the measuring instruments themselves. Where the relative errors were high, the majority of those instances were reliably attributed to factors related to model representation rather than the prediction algorithms themselves. These findings gave considerable support to the hypothesis regarding source visibility related errors (SVRE) that was formulated in Chapter 3. For the small number of high relative error predictions that could not be attributed to SVRE, it was not possible to find a single cause or relation to

model parameters. It is suggested that these might be due to any one of a number of *other* causes related to model representation, rather than the underlying accuracy of the *Radiance* program itself.

These could be any one or more of the following:

- The limited geometrical extent of the building model (Section 3.2.1).
- The uncertainty of the sky brightness distribution away from the CER - small bright clouds could cause significant variation in sky luminance at scales smaller that the 11˚ acceptance angle of the scanner.
- Marked changes in the sky brightness distribution during the sky scan - this can occur on bright days with fast moving patchy clouds.
- Marked variation in the values and character of the external ground reflectance due to rain or snow.
- Marked variation in the window transmission characteristics caused by dirt, heavy showers etc.

Accurate illuminance predictions were achieved using, in the main, fairly coarse ambient parameter settings. It is reasonable to assume therefore that comparable accuracy could also be attained for buildings of greater complexity than the BRE office, e.g. an office space adjacent to an atrium, Figure 4-47(a). There are, of course, qualifications to this assertion. Firstly, complex buildings are likely to require longer simulation times. Predicting the daylight illuminance levels for a very deep-plan space, such as the example given in Figure 4-47(b), is possible, if computationally very demanding. But note that for most practical daylighting purposes, useful levels of illumination are generally achieved after two or three diffuse light reflections; thereafter the higher order reflections add little to the overall total. For the very deep-plan space therefore, there is likely be little practical use in predicting what will be negligible levels of daylight illumination.

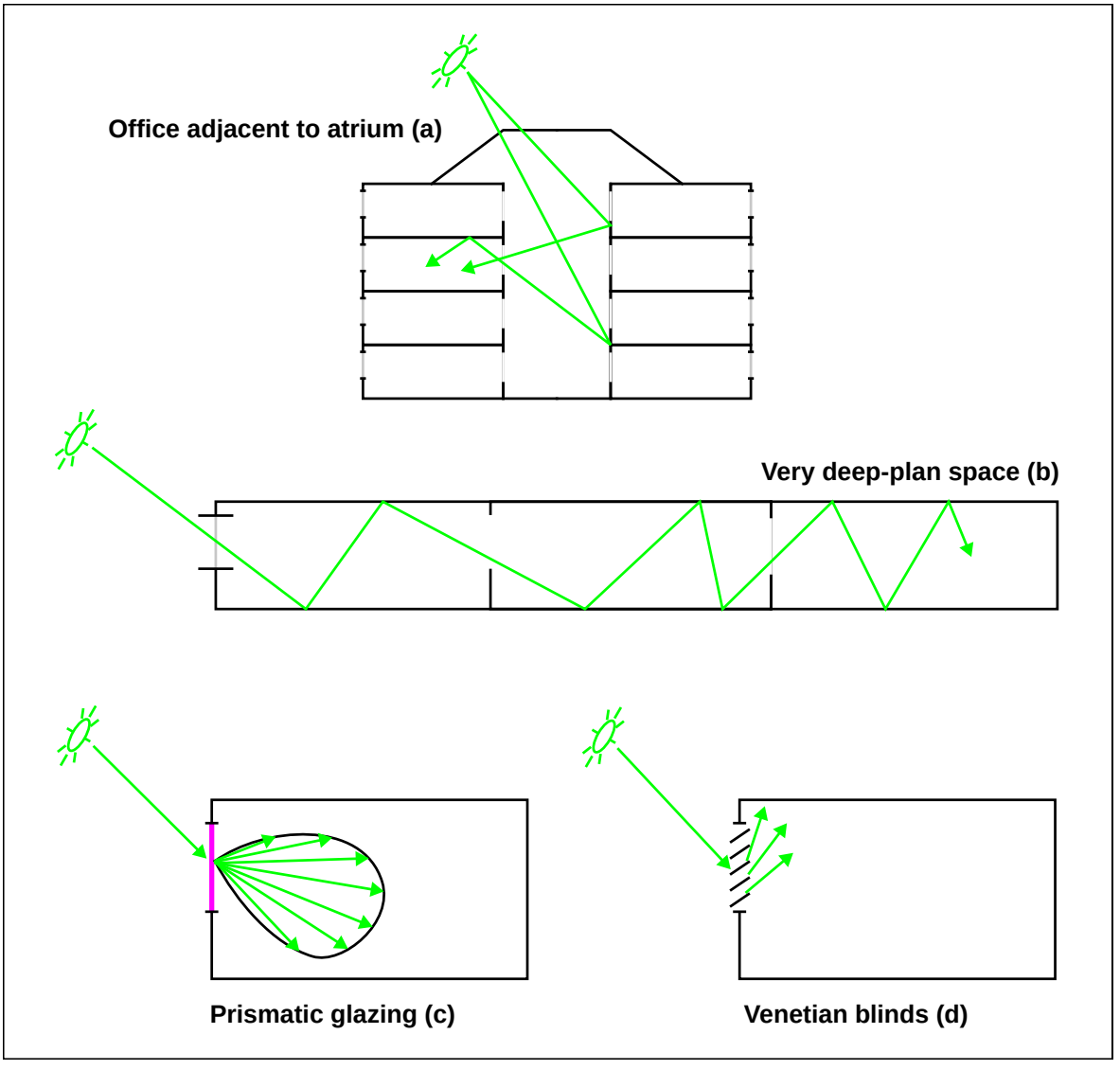

Figure 4-47. 'Complex buildings'

The modelling of so-called advanced glazing materials, such as prismatics (Figure 4-47c), pose other problems. To model these materials with any certainty, their optical properties must be adequately represented in the simulation. This generally means that the material's bi-directional transmission distribution function (BTDF) must be known and characterised in some way. The *Radiance* system has the capability to model advanced glazing materials based on empirical BTDFs. These quantities are only just being measured and their use in *Radiance* is not

straightforward. Even ‘common or garden’ venetian blinds can prove difficult to model because light transmission here depends on several reflections occurring over very small scales between the slats, Figure 4-47(d).

For overcast skies - where the circumsolar luminance is not an issue - the accuracy of the illuminance predictions must be considered to be very good. Accordingly, daylight factor predictions using the CIE overcast sky will have comparable accuracy. For all non-overcast skies however, the illuminance predictions for all those occasions when the circumsolar region is visible from the point of calculation must be considered to be potentially inaccurate. This is likely to be the case for any illuminance predictions resulting from sky luminance patterns that are based on scanner measurements comparable to those used for this study.

In the main, for the vast majority of practitioners, a daylight illumination analysis will be one based on daylight factors (Section 2.2.1). The daylight factor approach assumes a CIE overcast sky, i.e. no sun and no azimuthal anisotropy in the sky luminance. The daylight factor approach is based on a fixed ratio between the internal and the external illuminance. It has long been appreciated however that the ratio of internal to external illuminance varies greatly under real skies [Tregenza 83]. Thus the daylight factor approach can offer only a limited measure of the actually occurring daylight illumination levels. A more accurate evaluation of daylight provision would take into account all of the illuminance components - direct sun, direct sky and inter-reflected - resulting from a wide range of sky types that can be demonstrated to be representative of the naturally occurring climatic conditions for the appropriate locale. Techniques to achieve this goal are described, applied and tested in the following chapters.